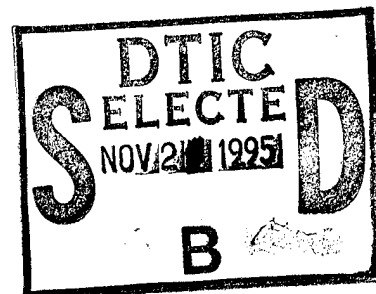


# NAVAL POSTGRADUATE SCHOOL MONTEREY, CALIFORNIA



## THESIS

**MODELING AND COMPUTER SIMULATION  
OF THE DYNAMIC RESPONSE AND FAILURE  
OF COMPOSITE STRUCTURES SUBJECTED  
TO SHOCK LOADING**

by

**Robert B. Burgio**

**June 1995**

**Thesis Advisor:**

**Young W. Kwon**

**Approved for public release; distribution is unlimited.**

**19951120 097**

**DTIC QUALITY INSPECTED 6**

REPORT DOCUMENTATION PAGE			Form Approved OMB No. 0704-0188	
Public reporting burden for this collection of information is estimated to average 1 hour per response, including the time for reviewing instruction, searching existing data sources, gathering and maintaining the data needed, and completing and reviewing the collection of information. Send comments regarding this burden estimate or any other aspect of this collection of information, including suggestions for reducing this burden, to Washington Headquarters Services, Directorate for Information Operations and Reports, 1215 Jefferson Davis Highway, Suite 1204, Arlington, VA 22202-4302, and to the Office of Management and Budget, Paperwork Reduction Project (0704-0188) Washington DC 20503.				
1. AGENCY USE ONLY (Leave blank)		2. REPORT DATE June 1995		3. REPORT TYPE AND DATES COVERED Engineer's Thesis
4. TITLE AND SUBTITLE MODELING AND COMPUTER SIMULATION OF THE DYNAMIC RESPONSE AND FAILURE OF COMPOSITE STRUCTURES SUBJECTED TO SHOCK LOADING			5. FUNDING NUMBERS	
6. AUTHOR(S) Burgio, Robert B.				
7. PERFORMING ORGANIZATION NAME(S) AND ADDRESS(ES) Naval Postgraduate School Monterey CA 93943-5000			8. PERFORMING ORGANIZATION REPORT NUMBER	
9. SPONSORING/MONITORING AGENCY NAME(S) AND ADDRESS(ES)			10. SPONSORING/MONITORING AGENCY REPORT NUMBER	
11. SUPPLEMENTARY NOTES The views expressed in this thesis are those of the author and do not reflect the official policy or position of the Department of Defense or the U.S. Government.				
12a. DISTRIBUTION/AVAILABILITY STATEMENT Approved for public release; distribution is unlimited.			12b. DISTRIBUTION CODE	
13. ABSTRACT (maximum 200 words)  The present thesis addresses the numerical modeling and analysis of the dynamic behavior and failure of composite structures subjected to either underwater shock or impact loading. A general purpose computer code was developed and tested for use on personal computers using both the finite element and boundary element techniques. The code can analyze general three-dimensional solid and shell structures. A wide variety of static and dynamic problems with known solutions are demonstrated to verify the accuracy of the code. This code is then used to model and analyze the dynamic response and failure of an unbalanced sandwich composite structure subjected to impact loading. Finally, the effects of composite layer smearing on the fluid-structure interaction are examined.				
14. SUBJECT TERMS Fluid-structure interaction, finite element, composite, underwater shock			15. NUMBER OF PAGES 72	
			16. PRICE CODE	
17. SECURITY CLASSIFI- CATION OF REPORT Unclassified	18. SECURITY CLASSIFI- CATION OF THIS PAGE Unclassified	19. SECURITY CLASSIFI- CATION OF ABSTRACT Unclassified	20. LIMITATION OF ABSTRACT UL	

Approved for public release; distribution is unlimited

MODELING AND COMPUTER SIMULATION OF THE DYNAMIC RESPONSE  
AND FAILURE OF COMPOSITE STRUCTURES SUBJECTED TO SHOCK  
LOADING

Robert B. Burgio, P.E.  
Lieutenant, United States Navy  
B.S.A.E., University of Maryland, College Park, 1987

Submitted in partial fulfillment  
of the requirements for the degrees of

**MASTER OF SCIENCE IN MECHANICAL ENGINEERING**  
and  
**MECHANICAL ENGINEER**

from the

NAVAL POSTGRADUATE SCHOOL  
June, 1995

Author:

*Robert B. Burgio*

Robert B. Burgio

Approved by:

*Young W. Kwon*

Young W. Kwon, Thesis Advisor

*Young S. Shin*

Young S. Shin, Second Reader

*Matthew D. Kelleher*

Matthew D. Kelleher, Chairman  
Department of Mechanical Engineering

Accession For	
NTIS GRA&I	<input checked="" type="checkbox"/>
DTIC TAB	<input type="checkbox"/>
Unannounced	<input type="checkbox"/>
Justification	
By	
Distribution/	
Availability Codes	
Dist	Avail and/or
A-1	Special



## **ABSTRACT**

The present thesis addresses the numerical modeling and analysis of the dynamic behavior and failure of composite structures subjected to either underwater shock or impact loading. A general purpose computer code was developed and tested for use on personal computers using both the finite element and boundary element techniques. The code can analyze general three-dimensional solid and shell structures. A wide variety of static and dynamic problems with known solutions are demonstrated to verify the accuracy of the code. This code is then used to model and analyze the dynamic response and failure of an unbalanced sandwich composite structure subjected to impact loading. Finally, the effects of composite layer smearing on the fluid-structure interaction are examined.



## TABLE OF CONTENTS

I.	INTRODUCTION . . . . .	1
II.	FINITE ELEMENT FORMULATION . . . . .	3
	A. STIFFNESS MATRIX . . . . .	3
	1. Shell Element . . . . .	3
	2. Solid Element . . . . .	13
	3. Assembly into Global Stiffness Matrix . . . . .	19
	B. MASS MATRIX . . . . .	19
	1. Shell Element . . . . .	19
	2. Solid Element . . . . .	20
	3. Assembly into Global Mass Matrix . . . . .	21
	C. DAMPING MATRIX . . . . .	21
III.	FLUID-STRUCTURE INTERACTION . . . . .	23
	A. GOVERNING EQUATIONS . . . . .	23
	B. FLUID MASS MATRIX DEVELOPMENT . . . . .	24
	C. STABILITY CONSIDERATIONS . . . . .	26
	D. NUMERICAL SOLUTION OF THE FLUID-STRUCTURE INTERACTION EQUATIONS . . . . .	28
IV.	CODE APPLICATIONS . . . . .	31
	A. VERIFICATION EXAMPLES . . . . .	31
	1. Free Vibration of a Dry, Isotropic Rod . . . . .	31
	2. Dry, Isotropic Plate Subjected to a Step Pressure Loading . . . . .	33
	3. Wet, Isotropic Rod Subjected to a Step Pressure Loading . . . . .	35
	4. Wet, Isotropic Plate Subjected to a Step Pressure Loading. . . . .	39
	5. Static Deflection of an Axisymmetric Cylinder . . . . .	40
	6. Static Deflection of an Angle-Ply Composite . . . . .	42
	7. Wet, Isotropic Sphere Subjected to a Step Pressure Loading . . . . .	43
	B. UNBALANCED SANDWICH COMPOSITE IMPACT STUDY . . . . .	46
	C. EFFECTS OF COMPOSITE LAYER SMEARING ON THE FLUID- STRUCTURE INTERACTION . . . . .	53
V.	CONCLUSION. . . . .	59

LIST OF REFERENCES . . . . .	61
INITIAL DISTRIBUTION LIST . . . . .	63



## I. INTRODUCTION

The U.S. Navy has been greatly interested in determining the effects of underwater explosions on the structural dynamics of ships and submarines since well before World War II. Until recently, ship shock trials and experimental tests on scale models had been the preferred means to obtain the required information. However, due to the high cost and environmental problems associated with underwater explosion tests and the tremendous increases in computer processing capability, computer simulations have become a widely accepted alternative to the experimental tests in determining the dynamic response and failure modes of submerged and partially submerged structures. These simulations can analyze scenarios which are far too dangerous to attempt with ship shock trials. Furthermore, they provide valuable insight into the design and shock qualification process resulting in more combat effective, survivable and cost effective ships and submarines.

Composite materials are beginning to see widespread use as major structural components of military vehicles. They are typically used to improve the stiffness-to-weight ratio or the strength-to-weight ratio of a structural member. The mechanical properties can be tailored based on the design requirement in a manner unavailable with conventional metals or alloys. While manufacturing difficulties and cost have limited their use in current ship and submarine hulls, they have great potential to significantly improve the performance of future classes of ships and submarines.

The objective of this study is to develop a general purpose finite element code for the structural analysis of composite materials subjected to either underwater shock or impact loading for use on the personal computer (PC) platform. Linear elastic behavior of the material is assumed for this study. At a later time, nonlinear effects can be added such as the damage progression in composite materials for example.

A brief overview of the finite element formulation used in this code is presented first followed by the development and solution of the fluid-structure interaction equations. Several code verification problems are then demonstrated followed by an

application of the code to a sandwich composite impact problem and a study of the effects of layer smearing on the fluid-structure interaction.

## II. FINITE ELEMENT FORMULATION

### A. STIFFNESS MATRIX

#### 1. Shell Element

When the thickness of a structure is small compared to its lateral dimension, computational efficiency can be gained by using a two-dimensional shell element in the formulation. A nine-noded, quadratic, isoparametric shell element [Ref 1] was selected for use in the finite element code and is shown in Fig. 2.1. Transverse shear deformation was included in the formulation which results in the phenomenon that straight lines originally normal to the undeformed shell midplane surface remain straight, but not necessarily normal to the deformed midplane surface. Deflections were assumed to be linear functions of the local coordinate in the thickness direction. One advantage of this nine-noded element over other four and eight-noded shell elements is that the central nodal point is very convenient when selecting a representative point for velocities and pressures on the surface of the element for use with the fluid-structure interaction calculations.

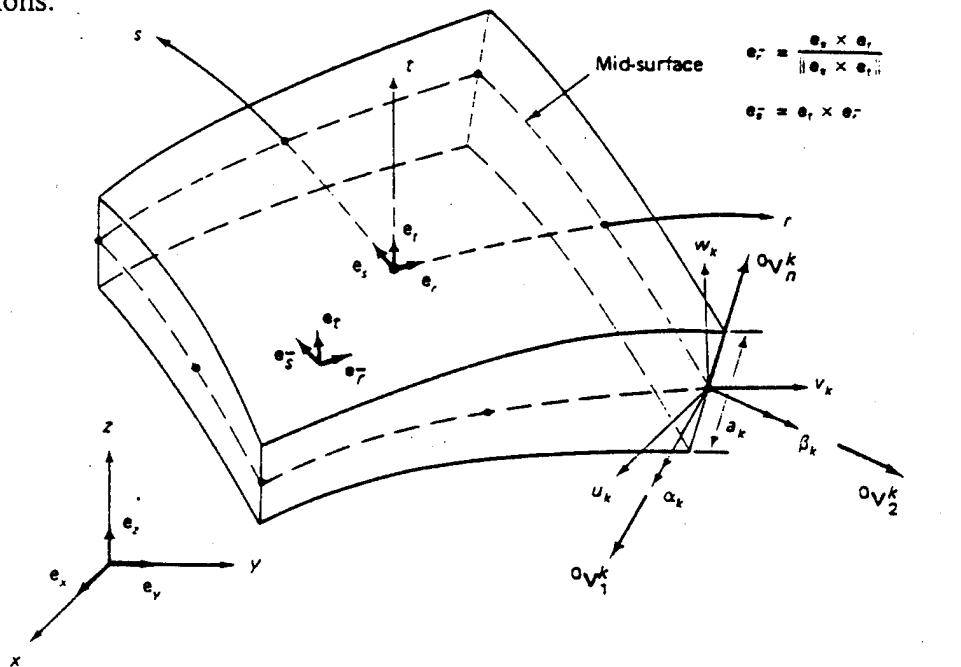


Figure 2.1 Nine Noded Isoparametric Shell Element (From Ref. 1)

Following the formulation outlined by Bathe [Ref. 1], the Cartesian coordinates of a point within the interior of the undeformed shell element with local coordinates  $r, s$  and  $t$  are given by

$$\begin{aligned} {}^0x(r,s,t) &= \sum_{k=1}^9 \left( {}^0x_k + \frac{t}{2} a_k {}^0V_{nx}^k \right) N_k(r,s) \\ {}^0y(r,s,t) &= \sum_{k=1}^9 \left( {}^0y_k + \frac{t}{2} a_k {}^0V_{ny}^k \right) N_k(r,s) \\ {}^0z(r,s,t) &= \sum_{k=1}^9 \left( {}^0z_k + \frac{t}{2} a_k {}^0V_{nz}^k \right) N_k(r,s) \end{aligned} \quad (2.1)$$

where  ${}^0x_k, {}^0y_k$  and  ${}^0z_k$  are the undeformed Cartesian coordinates of nodal point  $k$ ,  $a_k$  is the shell thickness at nodal point  $k$ ,  ${}^0V_n^k$  is the unit vector normal to the undeformed shell mid-surface at nodal point  $k$ , and  $N_k$  are the two-dimensional, bi-quadratic shape functions. Similarly, the Cartesian coordinates of a point within the deformed shell are

$$\begin{aligned} {}^1x(r,s,t) &= \sum_{k=1}^9 \left( {}^1x_k + \frac{t}{2} a_k {}^1V_{nx}^k \right) N_k(r,s) \\ {}^1y(r,s,t) &= \sum_{k=1}^9 \left( {}^1y_k + \frac{t}{2} a_k {}^1V_{ny}^k \right) N_k(r,s) \\ {}^1z(r,s,t) &= \sum_{k=1}^9 \left( {}^1z_k + \frac{t}{2} a_k {}^1V_{nz}^k \right) N_k(r,s) \end{aligned} \quad (2.2)$$

where  ${}^1x_k, {}^1y_k$  and  ${}^1z_k$  are the deformed Cartesian coordinates of nodal point  $k$  and  ${}^1V_n^k$  is the unit vector normal to the deformed shell mid-surface at nodal point  $k$ .

The shell displacement components are found by subtracting the undeformed coordinates of Eq. (2.1) from the deformed coordinates of Eq. (2.2) to yield

$$\begin{aligned} u(r,s,t) &= \sum_{k=1}^9 \left( u_k + \frac{t}{2} a_k V_{nx}^k \right) N_k(r,s) \\ v(r,s,t) &= \sum_{k=1}^9 \left( v_k + \frac{t}{2} a_k V_{ny}^k \right) N_k(r,s) \\ w(r,s,t) &= \sum_{k=1}^9 \left( w_k + \frac{t}{2} a_k V_{nz}^k \right) N_k(r,s) \end{aligned} \quad (2.3)$$

where  $V_n^k = {}^1V_n^k - {}^0V_n^k$  is the increment in the direction cosines of  ${}^0V_n^k$ .

The two-dimensional shape functions are obtained by appropriately multiplying together the one-dimensional, isoparametric shape functions which correspond to the local coordinates  $r$  and  $s$ . Assume that the one-dimensional elements have their first nodal point located at  $r = 1$ , the second at  $r = -1$ , and the third at  $r = 0$ . The quadratic shape functions for these three-noded elements in the local  $r$  coordinate are

$$N_{1r} = \frac{1}{2}(r^2 + r), \quad N_{2r} = \frac{1}{2}(r^2 - r), \quad N_{3r} = 1 - r^2 \quad (2.4)$$

Similarly, the one-dimensional shape functions in the local  $s$  coordinate are

$$N_{1s} = \frac{1}{2}(s^2 + s), \quad N_{2s} = \frac{1}{2}(s^2 - s), \quad N_{3s} = 1 - s^2 \quad (2.5)$$

Note that the  $k^{\text{th}}$  shape function is unity at the  $k^{\text{th}}$  node and zero at all the other nodes.

Multiplying these shape functions together yields the two dimensional shape functions shown in Table 2.1 below where the local coordinates of the  $k^{\text{th}}$  node have been included for completeness.

Nodal Point	$r$	$s$	Shape Function
1	1	1	$N_1 = N_{1r}N_{1s}$
2	-1	1	$N_2 = N_{2r}N_{1s}$
3	-1	-1	$N_3 = N_{2r}N_{2s}$
4	1	-1	$N_4 = N_{1r}N_{2s}$
5	0	1	$N_5 = N_{3r}N_{1s}$
6	-1	0	$N_6 = N_{2r}N_{3s}$
7	0	-1	$N_7 = N_{3r}N_{2s}$
8	1	0	$N_8 = N_{1r}N_{3s}$
9	0	0	$N_9 = N_{3r}N_{3s}$

**Table 2.1** Shell Element Shape Functions (see Fig. 2.1)

A convenient way to represent the direction cosines increment,  $V_n^k$  is to define two unit vectors,  ${}^0V_1^k$  and  ${}^0V_2^k$ , that are orthogonal both to  ${}^0V_n^k$  and to each other as shown in Fig. 2.1. Let  $V_n^k$  be a linear combination of  ${}^0V_1^k$  and  ${}^0V_2^k$  such that  $V_n^k = {}^0V_1^k\beta_k - {}^0V_2^k\alpha_k$

where  $\alpha_k$  and  $\beta_k$  represent the small angle rotations of the undeformed normal vector  ${}^0\mathbf{V}_n^k$  about the vectors  ${}^0\mathbf{V}_1^k$  and  ${}^0\mathbf{V}_2^k$ , respectively. Since there is no unique set of  ${}^0\mathbf{V}_1^k$  and  ${}^0\mathbf{V}_2^k$  orthogonal to  ${}^0\mathbf{V}_n^k$ , define  ${}^0\mathbf{V}_1^k = \mathbf{e}_y \times {}^0\mathbf{V}_n^k$  and let  ${}^0\mathbf{V}_2^k = {}^0\mathbf{V}_n^k \times {}^0\mathbf{V}_1^k$  where  $\mathbf{e}_y$  is a unit vector parallel to the y-axis. For the case that  ${}^0\mathbf{V}_n^k$  is parallel to  $\mathbf{e}_y$ , let  ${}^0\mathbf{V}_1^k = \mathbf{e}_z$ . Note that the unknown direction cosines increment,  $\mathbf{V}_n^k$ , has now been replaced with two unknown nodal rotations which are physically much more meaningful and make the application of slope boundary conditions simpler. Substituting for  $\mathbf{V}_n^k$  into Eq. (2.3) yields

$$\begin{aligned} u(r,s,t) &= \sum_{k=1}^9 \left( u_k + \frac{t}{2} a_k ({}^0V_{1x}^k \beta_k - {}^0V_{2x}^k \alpha_k) \right) N_k(r,s) \\ v(r,s,t) &= \sum_{k=1}^9 \left( v_k + \frac{t}{2} a_k ({}^0V_{1y}^k \beta_k - {}^0V_{2y}^k \alpha_k) \right) N_k(r,s) \\ w(r,s,t) &= \sum_{k=1}^9 \left( w_k + \frac{t}{2} a_k ({}^0V_{1z}^k \beta_k - {}^0V_{2z}^k \alpha_k) \right) N_k(r,s) \end{aligned} \quad (2.6)$$

In order to calculate the element strains, partial derivatives of the displacements need to be determined. For example; to find the longitudinal strain  $\epsilon_{xx} = \frac{\partial u}{\partial x}$ , the partial derivatives of  $u$  in the local  $(r,s,t)$  coordinates are undertaken first, then they are premultiplied by the inverse of the Jacobian matrix,  $\mathbf{J}$ , to determine the partial derivatives with respect to the Cartesian  $(x,y,z)$  coordinates. The displacement derivatives in local coordinates are given by

$$\begin{Bmatrix} \frac{\partial u}{\partial r} \\ \frac{\partial u}{\partial s} \\ \frac{\partial u}{\partial t} \end{Bmatrix} = \sum_{k=1}^9 \begin{bmatrix} \frac{\partial N_k}{\partial r} & 0 & 0 & \text{tg}_{1x}^k \frac{\partial N_k}{\partial r} & \text{tg}_{2x}^k \frac{\partial N_k}{\partial r} \\ \frac{\partial N_k}{\partial s} & 0 & 0 & \text{tg}_{1x}^k \frac{\partial N_k}{\partial s} & \text{tg}_{2x}^k \frac{\partial N_k}{\partial s} \\ 0 & 0 & 0 & g_{1x}^k N_k & g_{2x}^k N_k \end{bmatrix} \begin{Bmatrix} u_k \\ v_k \\ w_k \\ \alpha_k \\ \beta_k \end{Bmatrix}$$

$$\begin{aligned}
\begin{Bmatrix} \frac{\partial v}{\partial r} \\ \frac{\partial v}{\partial s} \\ \frac{\partial v}{\partial t} \end{Bmatrix} &= \sum_{k=1}^9 \begin{bmatrix} 0 & \frac{\partial N_k}{\partial r} & 0 & \text{tg}_{ly}^k \frac{\partial N_k}{\partial r} & \text{tg}_{2y}^k \frac{\partial N_k}{\partial r} \\ 0 & \frac{\partial N_k}{\partial s} & 0 & \text{tg}_{ly}^k \frac{\partial N_k}{\partial s} & \text{tg}_{2y}^k \frac{\partial N_k}{\partial s} \\ 0 & 0 & 0 & g_{ly}^k N_k & g_{2y}^k N_k \end{bmatrix} \begin{Bmatrix} u_k \\ v_k \\ w_k \\ \alpha_k \\ \beta_k \end{Bmatrix} \\
\begin{Bmatrix} \frac{\partial w}{\partial r} \\ \frac{\partial w}{\partial s} \\ \frac{\partial w}{\partial t} \end{Bmatrix} &= \sum_{k=1}^9 \begin{bmatrix} 0 & 0 & \frac{\partial N_k}{\partial r} & \text{tg}_{lz}^k \frac{\partial N_k}{\partial r} & \text{tg}_{2z}^k \frac{\partial N_k}{\partial r} \\ 0 & 0 & \frac{\partial N_k}{\partial s} & \text{tg}_{lz}^k \frac{\partial N_k}{\partial s} & \text{tg}_{2z}^k \frac{\partial N_k}{\partial s} \\ 0 & 0 & 0 & g_{lz}^k N_k & g_{2z}^k N_k \end{bmatrix} \begin{Bmatrix} u_k \\ v_k \\ w_k \\ \alpha_k \\ \beta_k \end{Bmatrix}
\end{aligned} \tag{2.7}$$

where  $g_1^k = -\frac{1}{2} a_k^0 V_2^k$  and  $g_2^k = \frac{1}{2} a_k^0 V_1^k$ . Note that the matrices in Eq. (2.7) have dimension  $3 \times 45$  for the nine-noded shell element.

The Jacobian matrix is given by

$$\mathbf{J} = \begin{bmatrix} \frac{\partial x}{\partial r} & \frac{\partial y}{\partial r} & \frac{\partial z}{\partial r} \\ \frac{\partial x}{\partial s} & \frac{\partial y}{\partial s} & \frac{\partial z}{\partial s} \\ \frac{\partial x}{\partial t} & \frac{\partial y}{\partial t} & \frac{\partial z}{\partial t} \end{bmatrix} \tag{2.8}$$

where the components in  $\mathbf{J}$  are determined by taking partial derivatives of Eq. (2.1)

$$\begin{aligned}
\frac{\partial x}{\partial r} &= \sum_{k=1}^9 \left( {}^0x_k + \frac{t}{2} a_k^0 V_{nx}^k \right) \frac{\partial N_k}{\partial r}, & \frac{\partial y}{\partial t} &= \sum_{k=1}^9 \frac{1}{2} a_k^0 V_{ny}^k N_k \\
\frac{\partial x}{\partial s} &= \sum_{k=1}^9 \left( {}^0x_k + \frac{t}{2} a_k^0 V_{nx}^k \right) \frac{\partial N_k}{\partial s}, & \frac{\partial w}{\partial r} &= \sum_{k=1}^9 \left( {}^0w_k + \frac{t}{2} a_k^0 V_{nz}^k \right) \frac{\partial N_k}{\partial r} \\
\frac{\partial x}{\partial t} &= \sum_{k=1}^9 \frac{1}{2} a_k^0 V_{nx}^k N_k, & \frac{\partial w}{\partial s} &= \sum_{k=1}^9 \left( {}^0x_w + \frac{t}{2} a_k^0 V_{nz}^k \right) \frac{\partial N_k}{\partial s} \\
\frac{\partial y}{\partial r} &= \sum_{k=1}^9 \left( {}^0y_k + \frac{t}{2} a_k^0 V_{ny}^k \right) \frac{\partial N_k}{\partial r}, & \frac{\partial w}{\partial t} &= \sum_{k=1}^9 \frac{1}{2} a_k^0 V_{nz}^k N_k \\
\frac{\partial y}{\partial s} &= \sum_{k=1}^9 \left( {}^0y_k + \frac{t}{2} a_k^0 V_{ny}^k \right) \frac{\partial N_k}{\partial s}, & &
\end{aligned} \tag{2.9}$$

The partial derivatives of the shape functions in Eq. 2.9 can easily be found as products of the one-dimensional shape functions and their derivatives in both the r and s local coordinates. The results are shown in Table 2.2 with the one-dimensional shape function derivatives determined by

$$\begin{aligned} \frac{\partial N_{1r}}{\partial r} &= r + \frac{1}{2}, & \frac{\partial N_{2r}}{\partial r} &= r - \frac{1}{2}, & \frac{\partial N_{3r}}{\partial r} &= -2r \\ \frac{\partial N_{1s}}{\partial s} &= s + \frac{1}{2}, & \frac{\partial N_{2s}}{\partial s} &= s - \frac{1}{2}, & \frac{\partial N_{3s}}{\partial s} &= -2s \end{aligned} \quad (2.10)$$

k	$\frac{\partial N_k}{\partial r}$	$\frac{\partial N_k}{\partial s}$
1	$\frac{\partial N_{1r}}{\partial r} N_{1s}$	$N_{1r} \frac{\partial N_{1s}}{\partial s}$
2	$\frac{\partial N_{2r}}{\partial r} N_{1s}$	$N_{2r} \frac{\partial N_{1s}}{\partial s}$
3	$\frac{\partial N_{2r}}{\partial r} N_{2s}$	$N_{2r} \frac{\partial N_{2s}}{\partial s}$
4	$\frac{\partial N_{1r}}{\partial r} N_{2s}$	$N_{1r} \frac{\partial N_{2s}}{\partial s}$
5	$\frac{\partial N_{3r}}{\partial r} N_{1s}$	$N_{3r} \frac{\partial N_{1s}}{\partial s}$
6	$\frac{\partial N_{2r}}{\partial r} N_{3s}$	$N_{2r} \frac{\partial N_{3s}}{\partial s}$
7	$\frac{\partial N_{3r}}{\partial r} N_{2s}$	$N_{3r} \frac{\partial N_{2s}}{\partial s}$
8	$\frac{\partial N_{1r}}{\partial r} N_{3s}$	$N_{1r} \frac{\partial N_{3s}}{\partial s}$
9	$\frac{\partial N_{3r}}{\partial r} N_{3s}$	$N_{3r} \frac{\partial N_{3s}}{\partial s}$

**Table 2.2** Shell Element Shape Function Derivatives

The displacement derivatives in Cartesian coordinates for a point in the shell element specified with local (r,s,t) coordinates then become



$$\begin{Bmatrix} \frac{\partial u}{\partial x} \\ \frac{\partial u}{\partial y} \\ \frac{\partial u}{\partial z} \end{Bmatrix} = [\mathbf{J}]^{-1} \begin{Bmatrix} \frac{\partial u}{\partial r} \\ \frac{\partial u}{\partial s} \\ \frac{\partial u}{\partial t} \end{Bmatrix}, \quad \begin{Bmatrix} \frac{\partial v}{\partial x} \\ \frac{\partial v}{\partial y} \\ \frac{\partial v}{\partial z} \end{Bmatrix} = [\mathbf{J}]^{-1} \begin{Bmatrix} \frac{\partial v}{\partial r} \\ \frac{\partial v}{\partial s} \\ \frac{\partial v}{\partial t} \end{Bmatrix}, \quad \begin{Bmatrix} \frac{\partial w}{\partial x} \\ \frac{\partial w}{\partial y} \\ \frac{\partial w}{\partial z} \end{Bmatrix} = [\mathbf{J}]^{-1} \begin{Bmatrix} \frac{\partial w}{\partial r} \\ \frac{\partial w}{\partial s} \\ \frac{\partial w}{\partial t} \end{Bmatrix} \quad (2.10)$$

which allows the strain-displacement matrix  $\mathbf{B}$  to be directly assembled where  $\mathbf{B}$  has dimension  $6 \times 45$  for the nine-noded shell element and is defined below.

$$\begin{Bmatrix} \epsilon_{xx} \\ \epsilon_{yy} \\ \epsilon_{zz} \\ \gamma_{xy} \\ \gamma_{yz} \\ \gamma_{xz} \end{Bmatrix} = \begin{Bmatrix} \frac{\partial u}{\partial x} \\ \frac{\partial u}{\partial y} \\ \frac{\partial u}{\partial z} \\ \frac{\partial v}{\partial x} + \frac{\partial u}{\partial y} \\ \frac{\partial w}{\partial x} + \frac{\partial v}{\partial z} \\ \frac{\partial y}{\partial x} + \frac{\partial z}{\partial z} \\ \frac{\partial w}{\partial x} + \frac{\partial u}{\partial z} \end{Bmatrix} = [\mathbf{B}] \begin{Bmatrix} u_1 \\ v_1 \\ w_1 \\ \alpha_1 \\ \beta_1 \\ u_2 \\ v_2 \\ \vdots \\ \alpha_9 \\ \beta_9 \end{Bmatrix} \quad (2.11)$$

The objective now is to determine the constitutive matrix relating the element strains to stresses,  $\sigma = \mathbf{D}_{\text{shell}} \epsilon$ . If the shell material is made up of orthotropic, thin laminae, then there are three coordinate systems to be concerned with: the global (x,y,z), local (r,s,t) and material (1,2,3) as shown in Fig. 2.2. Here it is assumed that the principal material axis, usually the one with the highest elastic modulus, is aligned in the "1" direction and the local "t" axis is coincident with the material "3" axis. The global coordinate axes are typically aligned along a major dimension of the structure.

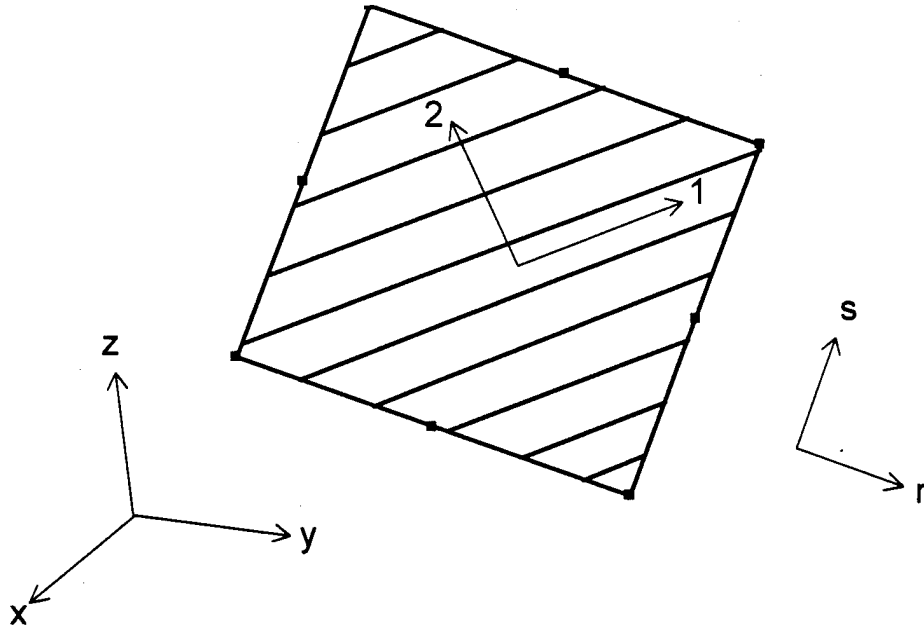


**Figure 2.2** Coordinate Systems for a Shell Element

The constitutive relation for an orthotropic lamina aligned in the material (1,2,3) coordinate system is given by  $\sigma_1 = \mathbf{D}_{\text{ortho}} \epsilon_1$ , which in expanded form becomes (Ref. 2)

$$\begin{Bmatrix} \sigma_{11} \\ \sigma_{22} \\ \sigma_{33} \\ \tau_{12} \\ \tau_{23} \\ \tau_{13} \end{Bmatrix} = \begin{bmatrix} Q_{11} & Q_{12} & 0 & 0 & 0 & 0 \\ Q_{12} & Q_{22} & 0 & 0 & 0 & 0 \\ 0 & 0 & 0 & 0 & 0 & 0 \\ 0 & 0 & 0 & Q_{66} & 0 & 0 \\ 0 & 0 & 0 & 0 & kQ_{44} & 0 \\ 0 & 0 & 0 & 0 & 0 & kQ_{55} \end{bmatrix} \begin{Bmatrix} \epsilon_{11} \\ \epsilon_{22} \\ \epsilon_{33} \\ \gamma_{12} \\ \gamma_{23} \\ \gamma_{13} \end{Bmatrix} \quad (2.12)$$

where the effects of shear deformation in the shell have been included. The normal stress and strain in the thickness direction,  $\sigma_3$  and  $\epsilon_3$ , are neglected in this shell formulation. The  $Q_{ij}$  factors are related to the material constants by

$$\begin{aligned} Q_{11} &= \frac{E_{11}}{1 - \nu_{12}\nu_{21}}, & Q_{12} &= \frac{\nu_{21}E_{11}}{1 - \nu_{12}\nu_{21}}, & Q_{22} &= \frac{E_{22}}{1 - \nu_{12}\nu_{21}} \\ Q_{44} &= G_{23}, & Q_{55} &= G_{31}, & Q_{66} &= G_{12} \end{aligned} \quad (2.13)$$

where  $E$  is the modulus of elasticity,  $\nu$  the Poisson ratio, and  $G$  the shear modulus. The shear correction factor,  $k = \frac{5}{6}$ , accounts for the fact that the finite element representation of the shell yields a constant transverse shear stress, whereas it actually has a non-constant distribution when calculated with continuum mechanics.

The next step is to transform the constitutive law from the material coordinate system to the local coordinate system. The material constitutive matrix  $\mathbf{D}_{\text{ortho}}$  can be converted into the local coordinate constitutive matrix  $\mathbf{D}_{\text{local}}$  with a tensor transformation of the form

$$\begin{aligned}\sigma_r &= \mathbf{D}_{\text{local}} \epsilon_r = \mathbf{T}^{-1} \mathbf{D}_{\text{ortho}} \mathbf{T} \epsilon_r \\ \mathbf{D}_{\text{local}} &= \mathbf{T}^{-1} \mathbf{D}_{\text{ortho}} \mathbf{T}\end{aligned}\quad (2.14)$$

where  $\sigma_r = [\sigma_{rr} \ \sigma_{ss} \ \sigma_{tt} \ \tau_{rs} \ \tau_{st} \ \tau_{rt}]^T$ ,  $\epsilon_r = [\epsilon_{rr} \ \epsilon_{ss} \ \epsilon_{tt} \ \gamma_{rs} \ \gamma_{st} \ \gamma_{rt}]^T$  and the transformation matrix  $\mathbf{T}$  is given by [Ref. 1]

$$\mathbf{T} = \begin{bmatrix} l_1^2 & m_1^2 & n_1^2 & l_1 m_1 & m_1 n_1 & l_1 n_1 \\ l_2^2 & m_2^2 & n_2^2 & l_2 m_2 & m_2 n_2 & l_2 n_2 \\ l_3^2 & m_3^2 & n_3^2 & l_3 m_3 & m_3 n_3 & l_3 n_3 \\ 2l_1 l_2 & 2m_1 m_2 & 2n_1 n_2 & l_1 m_2 + l_2 m_1 & m_1 n_2 + m_2 n_1 & l_1 n_2 + l_2 n_1 \\ 2l_2 l_3 & 2m_2 m_3 & 2n_2 n_3 & l_2 m_3 + l_3 m_2 & m_2 n_3 + m_3 n_2 & l_2 n_3 + l_3 n_2 \\ 2l_1 l_3 & 2m_1 m_3 & 2n_1 n_3 & l_1 m_3 + l_3 m_1 & m_1 n_3 + m_3 n_1 & l_1 n_3 + l_3 n_1 \end{bmatrix} \quad (2.15)$$

$$\begin{aligned}\text{where} \quad l_1 &= \cos(\mathbf{e}_{\bar{r}}, \mathbf{e}_1), & m_1 &= \cos(\mathbf{e}_{\bar{s}}, \mathbf{e}_1), & n_1 &= \cos(\mathbf{e}_{\bar{t}}, \mathbf{e}_1) \\ l_2 &= \cos(\mathbf{e}_{\bar{r}}, \mathbf{e}_2), & m_2 &= \cos(\mathbf{e}_{\bar{s}}, \mathbf{e}_2), & n_2 &= \cos(\mathbf{e}_{\bar{t}}, \mathbf{e}_2) \\ l_3 &= \cos(\mathbf{e}_{\bar{r}}, \mathbf{e}_3), & m_3 &= \cos(\mathbf{e}_{\bar{s}}, \mathbf{e}_3), & n_3 &= \cos(\mathbf{e}_{\bar{t}}, \mathbf{e}_3)\end{aligned}\quad (2.16)$$

The unit vectors  $\mathbf{e}_{\bar{r}}$  and  $\mathbf{e}_{\bar{s}}$  have been "orthogonalized" according to

$$\mathbf{e}_{\bar{r}} = \frac{\mathbf{e}_{\bar{s}} \times \mathbf{e}_{\bar{t}}}{\|\mathbf{e}_{\bar{s}} \times \mathbf{e}_{\bar{t}}\|}, \quad \mathbf{e}_{\bar{s}} = \mathbf{e}_{\bar{t}} \times \mathbf{e}_{\bar{r}} \quad (2.17)$$

since  $\mathbf{e}_r$ ,  $\mathbf{e}_s$ , and  $\mathbf{e}_t$  are in general not orthogonal. Assume that the material coordinate system is rotated counter-clockwise at an angle  $\theta$  with respect to the local coordinate system (with the material 3 axis coincident with the local  $t$  axis). Let  $m = \cos(\theta)$  and  $n = \sin(\theta)$ . The direction cosines of Eq. (2.16) reduce to  $l_1 = m$ ,  $l_2 = -n$ ,  $m_1 = n$ ,  $m_2 = m$ ,

$l_3=m_3=n_1=n_2=n_3=0$ . Substituting  $\mathbf{T}$  from Eq. (2.15) and  $\mathbf{D}_{\text{ortho}}$  from Eq. (2.12) into Eq. (2.14) yields

$$\mathbf{D}_{\text{local}} = \begin{bmatrix} \bar{Q}_{11} & \bar{Q}_{12} & 0 & \bar{Q}_{16} & 0 & 0 \\ \bar{Q}_{12} & \bar{Q}_{22} & 0 & \bar{Q}_{26} & 0 & 0 \\ 0 & 0 & 0 & 0 & 0 & 0 \\ \bar{Q}_{16} & \bar{Q}_{26} & 0 & \bar{Q}_{66} & 0 & 0 \\ 0 & 0 & 0 & 0 & k\bar{Q}_{44} & \bar{Q}_{45} \\ 0 & 0 & 0 & 0 & \bar{Q}_{45} & k\bar{Q}_{55} \end{bmatrix} \quad (2.18)$$

where

$$\begin{aligned} \bar{Q}_{11} &= Q_{11}m^4 + 2(Q_{12} + 2Q_{66})m^2n^2 + Q_{22}n^4 \\ \bar{Q}_{22} &= Q_{11}n^4 + 2(Q_{12} + 2Q_{66})m^2n^2 + Q_{22}m^4 \\ \bar{Q}_{44} &= Q_{44}m^2 + Q_{55}n^2 \\ \bar{Q}_{55} &= Q_{44}n^2 + Q_{55}m^2 \\ \bar{Q}_{66} &= (Q_{11} + Q_{22} - 2Q_{12} - 2Q_{66})m^2n^2 + Q_{66}(m^4 + n^4) \\ \bar{Q}_{12} &= (Q_{11} + Q_{22} - 4Q_{66})m^2n^2 + Q_{12}(m^4 + n^4) \\ \bar{Q}_{16} &= (Q_{11} - Q_{12} - 2Q_{66})m^3n + (Q_{12} - Q_{22} + 2Q_{66})mn^3 \\ \bar{Q}_{26} &= (Q_{11} - Q_{12} - 2Q_{66})mn^3 + (Q_{12} - Q_{22} + 2Q_{66})m^3n \\ \bar{Q}_{45} &= (Q_{55} - Q_{44})mn \end{aligned} \quad (2.19)$$

The next step is to transform the constitutive matrix from local coordinates to global (x,y,z) coordinates. This is done with another tensor transformation of the form

$$\begin{aligned} \sigma_x &= \mathbf{D}_{\text{shell}} \epsilon_x = \mathbf{T}^{-1} \mathbf{D}_{\text{local}} \mathbf{T} \epsilon_x \\ \mathbf{D}_{\text{shell}} &= \mathbf{T}^{-1} \mathbf{D}_{\text{local}} \mathbf{T} \end{aligned} \quad (2.20)$$

where  $\sigma_x = [\sigma_{xx} \ \sigma_{yy} \ \sigma_{zz} \ \tau_{xy} \ \tau_{yz} \ \tau_{xz}]^T$  and  $\epsilon_x = [\epsilon_{xx} \ \epsilon_{yy} \ \epsilon_{zz} \ \gamma_{xy} \ \gamma_{yz} \ \gamma_{xz}]^T$  and the tensor transformation matrix  $\mathbf{T}$  is also given by Eq. (2.15). The direction cosines for this case are determined by

$$\begin{aligned}
l_1 &= \cos(\mathbf{e}_x, \mathbf{e}_{\bar{r}}), & m_1 &= \cos(\mathbf{e}_y, \mathbf{e}_{\bar{r}}), & n_1 &= \cos(\mathbf{e}_z, \mathbf{e}_{\bar{r}}) \\
l_2 &= \cos(\mathbf{e}_x, \mathbf{e}_{\bar{s}}), & m_2 &= \cos(\mathbf{e}_y, \mathbf{e}_{\bar{s}}), & n_2 &= \cos(\mathbf{e}_z, \mathbf{e}_{\bar{s}}) \\
l_3 &= \cos(\mathbf{e}_x, \mathbf{e}_{\bar{t}}), & m_3 &= \cos(\mathbf{e}_y, \mathbf{e}_{\bar{t}}), & n_3 &= \cos(\mathbf{e}_z, \mathbf{e}_{\bar{t}})
\end{aligned} \tag{2.21}$$

We finally have enough information now to generate the element stiffness matrix  $\mathbf{k}_{\text{elem}}$ . This matrix relates element displacements and rotations to the applied element forces and moments according to

$$\mathbf{k}_{\text{elem}} \mathbf{d} = \mathbf{f}_{\text{elem}} \tag{2.22}$$

where  $\mathbf{d}$  is the vector of nodal displacements and rotations and has 45 components.  $\mathbf{f}_{\text{elem}}$  is the vector of applied nodal forces and moments and also has 45 components.  $\mathbf{k}_{\text{elem}}$  is determined by the volume integral

$$\mathbf{k}_{\text{elem}} = \int_V \mathbf{B}^T \mathbf{D}_{\text{shell}} \mathbf{B} dV \tag{2.23}$$

where  $dV = |\mathbf{J}| dr ds dt$ . The integration is carried out numerically using the Gauss quadrature method. Three integration points are needed in the  $r$  and  $s$  coordinates, while two points are sufficient in the  $t$  coordinate.

## 2. Solid Element

When components of a structure are not thin enough to justify use of the shell element formulated above, a three-dimensional solid element must be used in the finite element analysis. The 27 node, quadratic, isoparametric, solid (brick) element was chosen for use in the present finite element code and is shown in Fig. 2.3. Although it is a

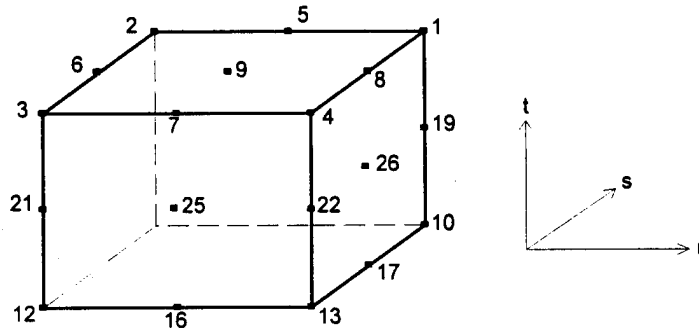


**Figure 2.3** 27-Noded Isoparametric Solid Element

computationally expensive element compared to other fewer noded solid elements, it has the advantage of providing easy compatibility when mixed with the 9-noded shell element.

The development of the solid element stiffness matrix closely parallels the development of the stiffness matrix for the shell element mentioned previously. Consider the element of Fig. 2.3 in the local coordinate system. The Cartesian coordinates of a point within the interior of the solid element are given by

$$x(r,s,t) = \sum_{k=1}^{27} x_k N_k, \quad y(r,s,t) = \sum_{k=1}^{27} y_k N_k, \quad z(r,s,t) = \sum_{k=1}^{27} z_k N_k \quad (2.24)$$

where  $x_k$ ,  $y_k$  and  $z_k$  are the undeformed Cartesian coordinates of nodal point  $k$  and  $N_k$  are the three-dimensional, quadratic shape functions. Similarly, the displacement components of a point within the solid element are given by

$$u(r,s,t) = \sum_{k=1}^{27} u_k N_k, \quad v(r,s,t) = \sum_{k=1}^{27} v_k N_k, \quad w(r,s,t) = \sum_{k=1}^{27} w_k N_k \quad (2.25)$$

where  $u_k$ ,  $v_k$  and  $w_k$  are the displacements of nodal point  $k$  (three displacement DOF per node). The three-dimensional shape functions are obtained by appropriately multiplying together the one-dimensional shape functions as was done previously for the shell element. The resulting shape functions are shown in Table 2.3 along with the local coordinates of the nodal points. The one-dimensional shape functions in the  $r$  and  $s$  coordinate systems were defined in Eqs. (2.4) and (2.5) while in the  $t$  coordinate system

$$N_{1t} = \frac{1}{2}(t^2 + t), \quad N_{2t} = \frac{1}{2}(t^2 - t) \quad \text{and} \quad N_{3t} = 1 - t^2 \quad (2.26)$$

Table 2.4 summarizes the shape function partial derivatives. The derivatives in the  $r$  and  $s$  coordinates were previously given by Eq. 2.10 while the derivatives in the  $t$  coordinate are given by

$$\frac{\partial N_{1r}}{\partial r} = r + \frac{1}{2}, \quad \frac{\partial N_{2r}}{\partial r} = r - \frac{1}{2} \quad \text{and} \quad \frac{\partial N_{3r}}{\partial r} = -2r \quad (2.27)$$

Nodal Point	r	s	t	Shape Function
1	1	1	1	$N_1 = N_{1r}N_{1s}N_{1t}$
2	-1	1	1	$N_2 = N_{2r}N_{1s}N_{1t}$
3	-1	-1	1	$N_3 = N_{2r}N_{2s}N_{1t}$
4	1	-1	1	$N_4 = N_{1r}N_{2s}N_{1t}$
5	0	1	1	$N_5 = N_{3r}N_{1s}N_{1t}$
6	-1	0	1	$N_6 = N_{2r}N_{3s}N_{1t}$
7	0	-1	1	$N_7 = N_{3r}N_{2s}N_{1t}$
8	1	0	1	$N_8 = N_{1r}N_{3s}N_{1t}$
9	0	0	1	$N_9 = N_{3r}N_{3s}N_{1t}$
10	1	1	2	$N_{10} = N_{1r}N_{1s}N_{2t}$
11	-1	1	2	$N_{11} = N_{2r}N_{1s}N_{2t}$
12	-1	-1	2	$N_{12} = N_{2r}N_{2s}N_{2t}$
13	1	-1	2	$N_{13} = N_{1r}N_{2s}N_{2t}$
14	0	1	2	$N_{14} = N_{3r}N_{1s}N_{2t}$
15	-1	0	2	$N_{15} = N_{2r}N_{3s}N_{2t}$
16	0	-1	2	$N_{16} = N_{3r}N_{2s}N_{2t}$
17	1	0	2	$N_{17} = N_{1r}N_{3s}N_{2t}$
18	0	0	2	$N_{18} = N_{3r}N_{3s}N_{2t}$
19	1	1	3	$N_{19} = N_{1r}N_{1s}N_{3t}$
20	-1	1	3	$N_{20} = N_{2r}N_{1s}N_{3t}$
21	-1	-1	3	$N_{21} = N_{2r}N_{2s}N_{3t}$
22	1	-1	3	$N_{22} = N_{1r}N_{2s}N_{3t}$
23	0	1	3	$N_{23} = N_{3r}N_{1s}N_{3t}$
24	-1	0	3	$N_{24} = N_{2r}N_{3s}N_{3t}$
25	0	-1	3	$N_{25} = N_{3r}N_{2s}N_{3t}$
26	1	0	3	$N_{26} = N_{1r}N_{3s}N_{3t}$
27	0	0	3	$N_{27} = N_{3r}N_{3s}N_{3t}$

**Table 2.3** Solid Element Shape Functions

k	$\frac{\partial N_k}{\partial r}$	$\frac{\partial N_k}{\partial s}$	$\frac{\partial N_k}{\partial t}$
1	$\frac{\partial N_{1r}}{\partial r} N_{1s} N_{1t}$	$N_{1r} \frac{\partial N_{1s}}{\partial s} N_{1t}$	$N_{1r} N_{1s} \frac{\partial N_{1t}}{\partial t}$
2	$\frac{\partial N_{2r}}{\partial r} N_{1s} N_{1t}$	$N_{2r} \frac{\partial N_{1s}}{\partial s} N_{1t}$	$N_{2r} N_{1s} \frac{\partial N_{1t}}{\partial t}$
3	$\frac{\partial N_{2r}}{\partial r} N_{2s} N_{1t}$	$N_{2r} \frac{\partial N_{2s}}{\partial s} N_{1t}$	$N_{2r} N_{2s} \frac{\partial N_{1t}}{\partial t}$
4	$\frac{\partial N_{1r}}{\partial r} N_{2s} N_{1t}$	$N_{1r} \frac{\partial N_{2s}}{\partial s} N_{1t}$	$N_{1r} N_{2s} \frac{\partial N_{1t}}{\partial t}$
5	$\frac{\partial N_{3r}}{\partial r} N_{1s} N_{1t}$	$N_{3r} \frac{\partial N_{1s}}{\partial s} N_{1t}$	$N_{3r} N_{1s} \frac{\partial N_{1t}}{\partial t}$
6	$\frac{\partial N_{2r}}{\partial r} N_{3s} N_{1t}$	$N_{2r} \frac{\partial N_{3s}}{\partial s} N_{1t}$	$N_{2r} N_{3s} \frac{\partial N_{1t}}{\partial t}$
7	$\frac{\partial N_{3r}}{\partial r} N_{2s} N_{1t}$	$N_{3r} \frac{\partial N_{2s}}{\partial s} N_{1t}$	$N_{3r} N_{2s} \frac{\partial N_{1t}}{\partial t}$
8	$\frac{\partial N_{1r}}{\partial r} N_{3s} N_{1t}$	$N_{1r} \frac{\partial N_{3s}}{\partial s} N_{1t}$	$N_{1r} N_{3s} \frac{\partial N_{1t}}{\partial t}$
9	$\frac{\partial N_{3r}}{\partial r} N_{3s} N_{1t}$	$N_{3r} \frac{\partial N_{3s}}{\partial s} N_{1t}$	$N_{3r} N_{3s} \frac{\partial N_{1t}}{\partial t}$
10	$\frac{\partial N_{1r}}{\partial r} N_{1s} N_{2t}$	$N_{1r} \frac{\partial N_{1s}}{\partial s} N_{2t}$	$N_{1r} N_{1s} \frac{\partial N_{2t}}{\partial t}$
11	$\frac{\partial N_{2r}}{\partial r} N_{1s} N_{2t}$	$N_{2r} \frac{\partial N_{1s}}{\partial s} N_{2t}$	$N_{2r} N_{1s} \frac{\partial N_{2t}}{\partial t}$
:	:	:	:
27	$\frac{\partial N_{3r}}{\partial r} N_{3s} N_{3t}$	$N_{3r} \frac{\partial N_{3s}}{\partial s} N_{3t}$	$N_{3r} N_{3s} \frac{\partial N_{3t}}{\partial t}$

**Table 2.4** Solid Element Shape Function Derivatives



In order to generate the strain displacement matrix, **B**, we first need to find the displacement derivatives in local coordinates and then perform a transformation to Cartesian coordinates. This transformation is accomplished through use of the Jacobian matrix. The elements in the Jacobian matrix, **J**, defined in Eq. (2.8) can be found by taking partial derivatives of Eq. (2.17) according to

$$\begin{aligned} \frac{\partial x}{\partial r} &= \sum_{k=1}^{27} x_k \frac{\partial N_k}{\partial r}, & \frac{\partial y}{\partial r} &= \sum_{k=1}^{27} y_k \frac{\partial N_k}{\partial r}, & \frac{\partial z}{\partial r} &= \sum_{k=1}^{27} z_k \frac{\partial N_k}{\partial r} \\ \frac{\partial x}{\partial s} &= \sum_{k=1}^{27} x_k \frac{\partial N_k}{\partial s}, & \frac{\partial y}{\partial s} &= \sum_{k=1}^{27} y_k \frac{\partial N_k}{\partial s}, & \frac{\partial z}{\partial s} &= \sum_{k=1}^{27} z_k \frac{\partial N_k}{\partial s} \\ \frac{\partial x}{\partial t} &= \sum_{k=1}^{27} x_k \frac{\partial N_k}{\partial t}, & \frac{\partial y}{\partial t} &= \sum_{k=1}^{27} y_k \frac{\partial N_k}{\partial t}, & \frac{\partial z}{\partial t} &= \sum_{k=1}^{27} z_k \frac{\partial N_k}{\partial t} \end{aligned} \quad (2.28)$$

The local coordinate displacement derivatives are determined by differentiating the displacements given in Eq. 2.25. The results are shown in matrix form as

$$\begin{aligned} \begin{Bmatrix} \frac{\partial u}{\partial r} \\ \frac{\partial u}{\partial s} \\ \frac{\partial u}{\partial t} \end{Bmatrix} &= \sum_{k=1}^{27} \begin{bmatrix} \frac{\partial N_k}{\partial r} & 0 & 0 \\ \frac{\partial N_k}{\partial s} & 0 & 0 \\ \frac{\partial N_k}{\partial t} & 0 & 0 \end{bmatrix} \begin{Bmatrix} u_k \\ v_k \\ w_k \end{Bmatrix} \\ \begin{Bmatrix} \frac{\partial v}{\partial r} \\ \frac{\partial v}{\partial s} \\ \frac{\partial v}{\partial t} \end{Bmatrix} &= \sum_{k=1}^{27} \begin{bmatrix} 0 & \frac{\partial N_k}{\partial r} & 0 \\ 0 & \frac{\partial N_k}{\partial s} & 0 \\ 0 & \frac{\partial N_k}{\partial t} & 0 \end{bmatrix} \begin{Bmatrix} u_k \\ v_k \\ w_k \end{Bmatrix} \\ \begin{Bmatrix} \frac{\partial w}{\partial r} \\ \frac{\partial w}{\partial s} \\ \frac{\partial w}{\partial t} \end{Bmatrix} &= \sum_{k=1}^{27} \begin{bmatrix} 0 & 0 & \frac{\partial N_k}{\partial r} \\ 0 & 0 & \frac{\partial N_k}{\partial s} \\ 0 & 0 & \frac{\partial N_k}{\partial t} \end{bmatrix} \begin{Bmatrix} u_k \\ v_k \\ w_k \end{Bmatrix} \end{aligned} \quad (2.29)$$

Premultiplying the matrices in Eq. (2.29) by the inverse of the Jacobian matrix gives the displacement derivatives in Cartesian coordinates

$$\begin{Bmatrix} \frac{\partial u}{\partial x} \\ \frac{\partial u}{\partial y} \\ \frac{\partial u}{\partial z} \end{Bmatrix} = [\mathbf{J}]^{-1} \begin{Bmatrix} \frac{\partial u}{\partial r} \\ \frac{\partial u}{\partial s} \\ \frac{\partial u}{\partial t} \end{Bmatrix}, \quad \begin{Bmatrix} \frac{\partial v}{\partial x} \\ \frac{\partial v}{\partial y} \\ \frac{\partial v}{\partial z} \end{Bmatrix} = [\mathbf{J}]^{-1} \begin{Bmatrix} \frac{\partial v}{\partial r} \\ \frac{\partial v}{\partial s} \\ \frac{\partial v}{\partial t} \end{Bmatrix}, \quad \begin{Bmatrix} \frac{\partial w}{\partial x} \\ \frac{\partial w}{\partial y} \\ \frac{\partial w}{\partial z} \end{Bmatrix} = [\mathbf{J}]^{-1} \begin{Bmatrix} \frac{\partial w}{\partial r} \\ \frac{\partial w}{\partial s} \\ \frac{\partial w}{\partial t} \end{Bmatrix} \quad (2.30)$$

which are used to assemble the size 6 x 81 strain-displacement matrix,  $\mathbf{B}$ , defined by

$$\begin{Bmatrix} \epsilon_{xx} \\ \epsilon_{yy} \\ \epsilon_{zz} \\ \gamma_{xy} \\ \gamma_{yz} \\ \gamma_{xz} \end{Bmatrix} = \begin{Bmatrix} \frac{\partial u}{\partial x} \\ \frac{\partial v}{\partial x} \\ \frac{\partial w}{\partial x} \\ \frac{\partial u}{\partial y} + \frac{\partial v}{\partial x} \\ \frac{\partial u}{\partial z} + \frac{\partial v}{\partial y} \\ \frac{\partial w}{\partial x} + \frac{\partial v}{\partial z} \end{Bmatrix} = [\mathbf{B}] \begin{Bmatrix} u_1 \\ v_1 \\ w_1 \\ u_2 \\ v_2 \\ w_2 \\ u_3 \\ \vdots \\ v_{27} \\ w_{27} \end{Bmatrix} \quad (2.31)$$

The next task is to find the stress-strain matrix,  $\mathbf{D}_{\text{brick}}$ . For the solid element we assume the material is isotropic. Thus, no tensor transformation is necessary to convert the constitutive matrix from local to Cartesian coordinates. The stress-strain matrix is

$$\mathbf{D}_{\text{brick}} = \frac{E(1-\nu)}{(1+\nu)(1-2\nu)} \begin{bmatrix} 1 & \frac{\nu}{1-\nu} & \frac{\nu}{1-\nu} & 0 & 0 & 0 \\ \frac{\nu}{1-\nu} & 1 & \frac{\nu}{1-\nu} & 0 & 0 & 0 \\ \frac{\nu}{1-\nu} & \frac{\nu}{1-\nu} & 1 & 0 & 0 & 0 \\ 0 & 0 & 0 & \frac{1-2\nu}{2(1-\nu)} & 0 & 0 \\ 0 & 0 & 0 & 0 & \frac{1-2\nu}{2(1-\nu)} & 0 \\ 0 & 0 & 0 & 0 & 0 & \frac{1-2\nu}{2(1-\nu)} \end{bmatrix} \quad (2.32)$$

where  $E$  is the modulus of elasticity and  $\nu$  is the Poisson ratio.

The shell element stiffness matrix can now be found with the volume integral

$$\mathbf{k}_{\text{elem}} = \int_V \mathbf{B}^T \mathbf{D}_{\text{brick}} \mathbf{B} dV \quad (2.33)$$

where  $dV = |J| dr ds dt$ . The integration is carried out numerically using the Gauss quadrature method. Three integration points are needed for each of the  $r$ ,  $s$  and  $t$  coordinates.

### 3. Assembly into Global Stiffness Matrix

Once the stiffness matrix is generated for an element, the next step is to assign the components of that matrix into the global stiffness matrix,  $\mathbf{K}_s$ . The relationship between the position of an entry in the element matrix and the corresponding position in the global matrix is obtained by conducting a table look-up in a connectivity table which is generated separately.

Due to symmetry and the highly banded nature of  $\mathbf{K}_s$ , an efficient way to store the components of it is through use of the skyline storage method [Refs. 1 & 9]. This scheme stores in a large vector only those entries which are within the "skyline" of the upper half of  $\mathbf{K}_s$ . The heights of the columns within the "skyline" are found by examining the connectivity table for the global DOF of interest and then locating the element attached to this global DOF which has the largest spread of global DOF associated with it. The height of the column is the difference between the largest and smallest DOF associated with this element.

## B. MASS MATRIX

### 1. Shell Element

In order to simplify the computations of generating the shell element mass matrix, a lumped mass model was used. This method entails assigning a fraction of the total element mass to each element node. This model has the added benefit of producing a diagonal mass matrix which tremendously reduces the storage requirements and the numerical operations involved when solving for the structural dynamic response.

The matrix  $\Phi$ , whose diagonal elements consist of the fractions of the total element mass carried by each node, is found by integrating over the area of the shell element in local coordinates according to

$$\Phi = \rho a \int_A \mathbf{N} \mathbf{N}^T dA \quad (2.34)$$

where  $\mathbf{N}$  is the column vector of shape functions,  $dA = |\mathbf{J}| dr ds$ ,  $a$  is the shell thickness and  $\rho$  is the mass density, assumed constant throughout the element. If the integration is carried out using the three-point Lobatto rule where the integration points correspond to the nodal points [Ref. 9], then the off-diagonal terms of  $\Phi$  become zero. For the case of a rectangular shell with constant thickness, the Jacobian matrix is constant throughout the shell. This produces diagonal components of  $\Phi$  equal to

$$\frac{\rho V_e}{36} \begin{bmatrix} 1 & 1 & 1 & 1 & 4 & 4 & 4 & 4 & 16 \end{bmatrix}$$

where  $V_e$  is the total volume of the element. Thus, the central node receives  $\frac{4}{9}$  of the total shell mass, each edge node receives  $\frac{1}{9}$  of the total and each corner node  $\frac{1}{36}$  of the total for the case of a rectangular element.

The mass contribution of each shell node is then assigned to the diagonal locations in the element mass matrix corresponding to each of the three translational degree-of-freedom (DOF) for that node. The remaining two diagonal locations in the matrix for each node correspond to moment of inertia terms which are neglected in this formulation (they are assigned small, non-zero values in order to keep the mass matrix non-singular). The result is a diagonal element mass matrix which can be stored as a vector of length 45.

## 2. Solid Element

The lumped mass model was also used to determine the element mass matrix for the solid element. The matrix  $\Phi$ , whose diagonal elements consist of the fraction of the total element mass carried by each node, is found by integrating over the volume of the solid element in local coordinates according to

$$\Phi = \rho \int_V \mathbf{N} \mathbf{N}^T dV \quad (2.35)$$

where  $dV = |\mathbf{J}| dr ds dt$  and  $\rho$  is the mass density, assumed constant throughout the element. For the case of a parallelepiped shaped element, the Jacobian matrix is constant throughout the element. This yields diagonal components of  $\Phi$  equal to

$$\frac{\rho V_e}{216} [1 \ 1 \ 1 \ 1 \ 4 \ 4 \ 4 \ 4 \ 16 \ 1 \ 1 \ 1 \ 1 \ 4 \ 4 \ 4 \ 4 \ 16 \ 4 \ 4 \ 4 \ 4 \ 16 \ 16 \ 16 \ 16 \ 64]$$

where  $V_e$  is the total volume of the element. Thus, the node at the center of the element receives  $\frac{8}{27}$  of the total element mass, each face node receives  $\frac{2}{27}$  of the total, each edge node receives  $\frac{1}{34}$  of the total and each corner node  $\frac{1}{216}$  of the total element mass. The mass contribution of each node is then assigned to the diagonal locations in the element mass matrix corresponding to each of the three translational DOF for that node. The result is a diagonal element mass matrix which can be stored as a vector of length 81.

### 3. Assembly into Global Mass Matrix

Since the element mass matrices are already diagonalized, their assembly into the global mass matrix,  $\mathbf{M}_s$ , is easily performed. The components of the element mass matrices are directly assigned into positions in the global mass matrix as specified by the connectivity table. The use of a diagonal global mass matrix requires very little storage and provides great computational efficiency in the transient response calculations.

## C. DAMPING MATRIX

The system damping matrix is formed as a linear combination of the global mass and stiffness matrices, termed Rayleigh damping, as follows

$$\mathbf{C}_s = \alpha \mathbf{M}_s + \beta \mathbf{K}_s \quad (2.36)$$

where  $\alpha$  and  $\beta$  are constants. If  $\alpha=0$  and  $\beta$  is nonzero then the damping tends to filter out high frequency components. Setting  $\beta=0$  and  $\alpha$  nonzero filters out low frequency

components. When  $\alpha$  and  $\beta$  are both nonzero then the damping is minimum at intermediate frequencies and becomes large at both low and high frequencies.

### III. FLUID-STRUCTURE INTERACTION

#### A. GOVERNING EQUATIONS

When a structure is submerged in a fluid and subjected to an incident acoustic wave, the resulting structural motion affects the strength of the scattered pressure wave. In addition, changes in the scattered pressure strength affect the dynamic response of the structure. Hence, the structural motion is coupled to the scattered fluid pressure. The governing equations for the fluid-structure response can thus be represented as a set of coupled, linear, ordinary differential equations.

Application of Newton's second law to a structure submerged in an infinite acoustic medium results in

$$\mathbf{M}_s \ddot{\mathbf{x}} + \mathbf{C}_s \dot{\mathbf{x}} + \mathbf{K}_s \mathbf{x} = -\mathbf{G} \mathbf{A}_f (\mathbf{p}_I + \mathbf{p}_s) \quad (3.1)$$

where  $\mathbf{M}_s$ ,  $\mathbf{C}_s$  and  $\mathbf{K}_s$  are the structural mass, damping and stiffness matrices, respectively,  $\mathbf{x}$  is the structural displacement vector,  $\mathbf{A}_f$  is a diagonal matrix of the fluid element areas,  $\mathbf{p}_I$  is the vector of incident pressures and  $\mathbf{p}_s$  is the vector of scattered pressures.  $\mathbf{G}$  is the pressure/force compatibility matrix which assigns the fluid pressures acting on the wet structure fluid nodes to forces acting on the structural nodes. The  $\mathbf{G}$  matrix also relates the fluid particle velocities and structural nodal velocities according to

$$\mathbf{G}^T \dot{\mathbf{x}} = \mathbf{u}_I + \mathbf{u}_s \quad (3.2)$$

where  $\mathbf{u}_I$  is the incident normal fluid particle velocity and  $\mathbf{u}_s$  is the scattered (reflected) normal fluid particle velocity.

The scattered pressure in Eq. (3.1) can be obtained by applying a doubly asymptotic approximation (DAA) which is based upon the representation of surface motion as a linear combination of orthogonal fluid boundary modes. The simplest approximation, DAA<sub>1</sub>, as given by Geers [Ref. 18] is

$$\mathbf{M}_f \dot{\mathbf{p}}_s + \rho c \mathbf{A}_f \mathbf{p}_s = \rho c \mathbf{M}_f \dot{\mathbf{u}}_s \quad (3.3)$$

where  $\mathbf{M}_f$  is the fluid mass matrix,  $\rho$  is the fluid density and  $c$  is the speed of sound in the fluid. Solving Eq. (3.2) for  $\mathbf{u}_s$  and substituting into Eq. (3.3) yields

$$\mathbf{M}_f \dot{\mathbf{p}}_s + \rho c \mathbf{A}_f \mathbf{p}_s = \rho c \mathbf{M}_f (\mathbf{G}^T \ddot{\mathbf{x}} - \dot{\mathbf{u}}_I) \quad (3.4)$$

Eqs. (3.1) and (3.4) are the governing equations for the fluid-structure interaction problem with unknown variables  $\mathbf{x}$  and  $\mathbf{p}_s$ .

## B. FLUID MASS MATRIX DEVELOPMENT

The fluid mass matrix,  $\mathbf{M}_f$ , is produced by using a boundary element formulation to solve Laplace's equation for an incompressible, inviscid, irrotational and infinite fluid subjected to motion of the structure's wet surface.  $\mathbf{M}_f$  is determined solely from the geometrical characteristics of the finite-element representation of the wet surface of the body and is fully populated. The governing equations for fluid motion are [Ref 4]

$$\begin{aligned}\nabla^2 \phi &= 0 && \text{in the fluid domain} \\ \frac{\partial \phi}{\partial n} &= -u && \text{on the structure's surface} \\ \nabla \phi &= 0 && \text{infinitely far from the structure}\end{aligned}\tag{3.5}$$

where  $\phi$  is the velocity potential,  $n$  is a unit vector normal to the structure surface and  $u$  is the normal velocity of the structure's surface.

A simple source formulation [Ref. 4] can be used to solve Eq. (3.5) according to

$$\begin{aligned}\phi(p) &= \int_s \frac{\sigma(q)}{r(p,q)} dS(q) \\ \frac{\partial \phi}{\partial n}(p) &= -2\pi\sigma(p) + \int_s \frac{\sigma(q) \cos\theta(p,q)}{r^2(p,q)} dS(q)\end{aligned}\tag{3.6}$$

where  $r(p,q)$  is the magnitude of the vector  $\mathbf{r}(p,q)$  from the receiver, point  $p$ , to the transmitter, point  $q$ ;  $\sigma(q)$  is the source strength;  $S$  is the wetted structural surface; and  $\theta$  is the angle between  $\mathbf{r}(p,q)$  and  $\mathbf{n}(p)$ . The geometry is shown in Fig. 3.1. The kinetic

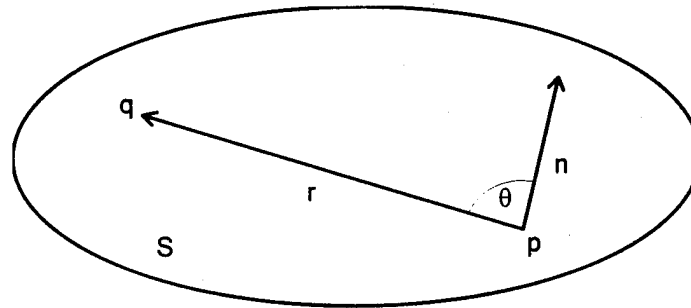


Figure 3.1. Source Formulation Geometry



energy of the fluid can be expressed as

$$T_f = -\frac{1}{2} \rho \int_S \frac{\partial \phi}{\partial n}(\mathbf{p}) \phi(\mathbf{p}) dS(\mathbf{p}) \quad (3.7)$$

where  $\rho$  is the fluid density.

If it is assumed that the source strength is constant throughout each fluid element, then Eqs. (3.6) and (3.7) can be written in matrix form as

$$\phi(\mathbf{p}) = \mathbf{B}(\mathbf{p})\sigma \quad (3.8)$$

$$\frac{\partial \phi}{\partial n}(\mathbf{p}) = -\mathbf{C}(\mathbf{p})\sigma \quad (3.9)$$

$$T_f = -\frac{1}{2} \rho \int_S \left[ \frac{\partial \phi}{\partial n}(\mathbf{p}) \right]^T dS(\mathbf{p}) \phi(\mathbf{p}) \quad (3.10)$$

where the elements of  $\mathbf{B}$  and  $\mathbf{C}$  are given by

$$b_{ij}(\mathbf{p}_i) = \int_{s_j} \frac{dS(\mathbf{q}_j)}{r(\mathbf{p}_i, \mathbf{q}_j)} \quad (3.11)$$

$$c_{ij}(\mathbf{p}_i) = 2\pi\delta_{ij} - \int_{s_j} \frac{\cos\theta(\mathbf{p}_i, \mathbf{q}_j)}{r^2(\mathbf{p}_i, \mathbf{q}_j)} dS(\mathbf{q}_j) \quad (3.12)$$

Using the  $I_1$  scheme described in Ref. 4, Eqs. 3.11 and 3.12 can be simplified to

$$\begin{aligned} b_{ii} &= 2\sqrt{\pi a_i} \\ b_{ij} &= \frac{a_j}{r_{ij}} \\ c_{ii} &= 2\pi \\ c_{ij} &= b_{ij} \frac{\cos\theta_{ij}}{r_{ij}} \end{aligned} \quad (3.13)$$

where  $r_{ij}$  is the straight-line distance from the centroid of the  $i^{\text{th}}$  element to the centroid of the  $j^{\text{th}}$  element,  $a_i$  is the surface area of the  $i^{\text{th}}$  element and  $\theta_{ij}$  is the angle between the vector corresponding to  $r_{ij}$  and the  $i^{\text{th}}$  element's unit normal.

The source strength can now be found by solving Eq. (3.9) for  $\sigma$

$$\sigma = \mathbf{C}^{-1}(\mathbf{p}')\mathbf{u} \quad (3.14)$$

where  $\mathbf{p}'$  is any desired set of control points and the control point normal velocity  $\mathbf{u}$  is equal to  $-\frac{\partial \phi}{\partial n}(\mathbf{p}')$ . Eliminating  $\sigma$  in Eq. (3.8) and the transpose of Eq. (3.9) yields

$$\begin{aligned}\phi(\mathbf{p}) &= \mathbf{B}(\mathbf{p})\mathbf{C}^{-1}(\mathbf{p}')\mathbf{u} \\ \left[ \frac{\partial \phi}{\partial \mathbf{n}}(\mathbf{p}) \right]^T &= -\mathbf{u}^T \mathbf{C}^{-T}(\mathbf{p}') \mathbf{C}^T(\mathbf{p})\end{aligned}\quad (3.15)$$

We can now obtain a more useful expression for the fluid kinetic energy by substituting Eq. (3.15) into Eq. (3.10) to produce

$$\mathbf{T}_f = \frac{1}{2} \rho \mathbf{u}^T \mathbf{C}^{-T}(\mathbf{p}') \left[ \int_S \mathbf{C}^T(\mathbf{p}) dS(\mathbf{p}) \mathbf{B}(\mathbf{p}) \right] \mathbf{C}^{-1}(\mathbf{p}') \mathbf{u} \quad (3.16)$$

If we use one point integration for the integral in Eq. (3.16) with  $\mathbf{p} = \mathbf{p}'$  then the fluid kinetic energy can be expressed as

$$\mathbf{T}_f = \frac{1}{2} \rho \mathbf{u}^T \mathbf{A}_f \mathbf{B} \mathbf{C}^{-1} \mathbf{u} \quad (3.17)$$

where  $\mathbf{A}_f$  is a diagonal matrix of the fluid element areas. Let  $\mathbf{E} = \mathbf{A}_f \mathbf{B} \mathbf{C}^{-1}$  and define the fluid mass matrix by

$$\mathbf{T}_f = \frac{1}{2} \mathbf{u}^T \mathbf{M}_f \mathbf{u} \quad (3.18)$$

Then the symmetric fluid mass matrix can now be expressed as

$$\mathbf{M}_f = \frac{1}{2} \rho (\mathbf{E} + \mathbf{E}^T) \quad (3.19)$$

## C. STABILITY CONSIDERATIONS

The solution of the interaction Eqs. (3.1) and (3.4) can be further stabilized with respect to the choice of time increment by injecting one of the coupled equations into the other as recommended by DeRuntz [Ref. 3]. Solving Eq. (3.1) for  $\ddot{\mathbf{x}}$ , substituting into Eq. (3.4) and premultiplying both sides of the resulting equation by  $\mathbf{A}_f \mathbf{M}_f^{-1}$  yields

$$\begin{aligned}\mathbf{A}_f \dot{\mathbf{p}}_s + (\rho c \mathbf{A}_f \mathbf{M}_f^{-1} \mathbf{A}_f) \mathbf{p}_s &= -\rho c \mathbf{A}_f \mathbf{G}^T \mathbf{M}_s^{-1} \mathbf{C}_s \dot{\mathbf{x}} - \rho c \mathbf{A}_f \mathbf{G}^T \mathbf{M}_s^{-1} \mathbf{K}_s \mathbf{x} \\ &\quad - (\rho c \mathbf{A}_f \mathbf{G}^T \mathbf{M}_s^{-1} \mathbf{G} \mathbf{A}_f) \mathbf{p}_I - (\rho c \mathbf{A}_f \mathbf{G}^T \mathbf{M}_s^{-1} \mathbf{G} \mathbf{A}_f) \mathbf{p}_s - \rho c \mathbf{A}_f \dot{\mathbf{u}}_I\end{aligned}\quad (3.20)$$

Defining  $\mathbf{D}_{fI} = \rho c \mathbf{A}_f \mathbf{M}_f^{-1} \mathbf{A}_f$ ,  $\mathbf{D}_s = \rho c \mathbf{A}_f \mathbf{G}^T \mathbf{M}_s^{-1} \mathbf{G} \mathbf{A}_f$ ,  $\mathbf{D}_I = \mathbf{D}_{fI} + \mathbf{D}_s$  and  $\mathbf{D}_2 = -\rho c \mathbf{A}_f \mathbf{G}^T \mathbf{M}_s^{-1}$  yields the augmented, second fluid-structure interaction equation

$$\mathbf{A}_f \dot{\mathbf{p}}_s + \mathbf{D}_I \mathbf{p}_s = \mathbf{D}_2 (\mathbf{C}_s \dot{\mathbf{x}} + \mathbf{K}_s \mathbf{x}) - \mathbf{D}_s \mathbf{p}_I - \rho c \mathbf{A}_f \dot{\mathbf{u}}_I \quad (3.21)$$

The presence of the  $\dot{\mathbf{u}}_I$  term in Eq. (3.21) presents numerical difficulties when an incident shock wave is modeled. This can be alleviated for a spherical incident wave by defining a modified pressure vector

$$\mathbf{p}_M = \mathbf{p}_S + \Gamma \mathbf{p}_I \quad (3.22)$$

where  $\Gamma$  is a diagonal matrix of the direction cosine elements  $\gamma_i$  and  $\gamma_i = \cos(\Phi_i)$ .  $\Phi_i$  is the angle between a vector coincident with  $R_i$ , the distance from the origin of the incident spherical wave to the  $i^{\text{th}}$  fluid node on the wet surface of the structure, and  $\mathbf{n}_i$ , the wet surface normal vector of the  $i^{\text{th}}$  fluid node as shown in Fig. 3.2.

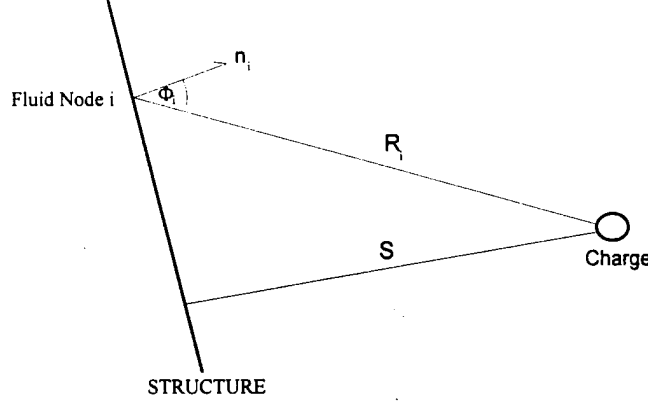


Figure 3.2. Charge Geometry

The wet surface pressure,  $\mathbf{p}_{\text{Tot}}$ , is now given by

$$\mathbf{p}_{\text{Tot}} = \mathbf{p}_I + \mathbf{p}_S = (\mathbf{I} - \Gamma) \mathbf{p}_I + \mathbf{p}_M \quad (3.23)$$

Solving Eq. (3.22) for  $\mathbf{p}_S$  and substituting into Eq. (3.21) produces the modified, augmented fluid-structure interaction equations

$$\mathbf{M}_s \ddot{\mathbf{x}} + \mathbf{C}_s \dot{\mathbf{x}} + \mathbf{K}_s \mathbf{x} = -\mathbf{G} \mathbf{A}_f (\mathbf{p}_M + (\mathbf{I} - \Gamma) \mathbf{p}_I) \quad (3.24)$$

$$\mathbf{A}_f \dot{\mathbf{p}}_M + \mathbf{D}_1 \mathbf{p}_M = \mathbf{D}_2 (\mathbf{C}_s \dot{\mathbf{x}} + \mathbf{K}_s \mathbf{x}) + (\mathbf{D}_1 \Gamma - \mathbf{D}_s) \mathbf{p}_I + \mathbf{A}_f \Gamma \dot{\mathbf{p}}_I - \rho c \mathbf{A}_f \dot{\mathbf{u}}_I \quad (3.25)$$

For a spherical wave in a homogeneous fluid, the incident wave pressure at the  $i^{\text{th}}$  fluid node,  $p_{I_i}$ , is related to the incident wave fluid particle velocity at the  $i^{\text{th}}$  fluid node,  $u_{I_i}$ , and the incident wave pressure at the standoff distance,  $p_I$ , by the following

$$\dot{u}_{I_i}(t) = \gamma_i \left( \frac{1}{\rho c} \dot{p}_{I_i}(t) + \frac{1}{\rho R_i} p_{I_i}(t) \right) \quad (3.26)$$

$$p_{I_i}(t) = \frac{S}{R_i} p_I \left( t - \frac{R_i - S}{c} \right) \quad (3.27)$$

where  $R$  is a diagonal matrix of the radii  $R_i$  and  $S$ , the standoff distance, is defined to be the distance from the origin of the spherical wave to the nearest point on the wet structure. Converting Eq. (3.26) into vector format and rearranging to solve for  $\dot{p}_I$  yields

$$\dot{p}_I = \rho c \Gamma^{-1} \dot{u}_I - c R^{-1} p_I \quad (3.28)$$

which, when substituted into Eq. (3.25), causes the terms involving  $\dot{u}_I$  to cancel out producing

$$A_f \dot{p}_M + D_I p_M = D_2 (C_s \dot{x} + K_s x) + (D_I \Gamma - D_s - c A_f R^{-1} \Gamma) p_I \quad (3.29)$$

Defining  $H = D_I \Gamma - D_s - c A_f R^{-1} \Gamma$  yields

$$A_f \dot{p}_M + D_I p_M = D_2 (C_s \dot{x} + K_s x) - H p_I \quad (3.30)$$

## D. NUMERICAL SOLUTION OF THE FLUID-STRUCTURE INTERACTION EQUATIONS

The solution of the modified, augmented, fluid-structure interaction Eqs. (3.24) and (3.30) is obtained by using a staggered solution procedure in conjunction with the central finite difference method. Assuming the structure is initially at rest with initial conditions  $x^0 = \dot{x}^0 = \ddot{x}^0 = \frac{\Delta t}{2} = p_M^0 = 0$  and assuming the incident pressure,  $p_I$ , is known at all times, the first calculation is to find the initial acceleration vector. Solving Eq. (3.24) for  $\ddot{x}$  at time zero, then integrating for velocity and displacement for the first time step yields

$$\begin{aligned} \ddot{x}^0 &= -M_s^{-1} (G A_f (p_M^0 + (I - \Gamma) p_I^0) + C_s \dot{x}^0 + K_s x^0) = -M_s^{-1} G A_f (I - \Gamma) p_I^0 \\ \dot{x}^{\frac{\Delta t}{2}} &= \dot{x}^0 + \ddot{x}^0 \Delta t = \ddot{x}^0 \Delta t \\ x^{\Delta t} &= x^0 + \dot{x}^{\frac{\Delta t}{2}} \Delta t = \dot{x}^{\frac{\Delta t}{2}} \Delta t \\ \ddot{x}^{\frac{\Delta t}{2}} &= \frac{1}{2} (\ddot{x}^0 + \ddot{x}^{\Delta t}) \end{aligned} \quad (3.31)$$

Applying Eq. (3.30) over the first time step yields

$$A_f \dot{p}_M^{\frac{\Delta t}{2}} + D_I p_M^{\frac{\Delta t}{2}} = D_2 \left( C_s \dot{x}^{\frac{\Delta t}{2}} + K_s x^{\frac{\Delta t}{2}} \right) - H p_I^{\frac{\Delta t}{2}} \quad (3.32)$$

Substituting  $\dot{p}_M^{\frac{\Delta t}{2}} = \frac{1}{\Delta t} (p_M^{\Delta t} - p_M^0)$  and  $p_M^{\frac{\Delta t}{2}} = \frac{1}{2} (p_M^0 + p_M^{\Delta t})$  into Eq. (3.32) produces

$$\frac{1}{\Delta t} \mathbf{A}_f (\mathbf{p}_M^{\Delta t} - \mathbf{p}_M^0) + \frac{1}{2} \mathbf{D}_1 (\mathbf{p}_M^0 + \mathbf{p}_M^{\Delta t}) = \mathbf{D}_2 \left( \mathbf{C}_s \dot{\mathbf{x}}^{\frac{\Delta t}{2}} + \mathbf{K}_s \mathbf{x}^{\frac{\Delta t}{2}} \right) - \mathbf{H} \mathbf{p}_I^{\frac{\Delta t}{2}} \quad (3.33)$$

which, after solving for the modified pressure at time  $\Delta t$ , gives

$$\mathbf{p}_M^{\Delta t} = \left( \frac{1}{\Delta t} \mathbf{A}_f + \frac{1}{2} \mathbf{D}_1 \right)^{-1} \left( \frac{1}{\Delta t} \mathbf{A}_f - \frac{1}{2} \mathbf{D}_1 \right) \mathbf{p}_M^0 + \left( \frac{1}{\Delta t} \mathbf{A}_f + \frac{1}{2} \mathbf{D}_1 \right)^{-1} \mathbf{D}_2 \left( \mathbf{C}_s \dot{\mathbf{x}}^{\frac{\Delta t}{2}} + \mathbf{K}_s \mathbf{x}^{\frac{\Delta t}{2}} \right) - \left( \frac{1}{\Delta t} \mathbf{A}_f + \frac{1}{2} \mathbf{D}_1 \right)^{-1} \mathbf{H} \mathbf{p}_I^{\frac{\Delta t}{2}} \quad (3.34)$$

$$\text{Let } \mathbf{D}_3 = \left( \frac{1}{\Delta t} \mathbf{A}_f + \frac{1}{2} \mathbf{D}_1 \right)^{-1}, \quad \mathbf{D}_4 = \frac{1}{\Delta t} \mathbf{A}_f - \frac{1}{2} \mathbf{D}_1, \quad \mathbf{D}_5 = \mathbf{D}_3 \mathbf{D}_4, \quad \mathbf{D}_6 = \mathbf{D}_3 \mathbf{D}_2, \quad \mathbf{D}_7 = -\mathbf{D}_3 \mathbf{H}$$

$$\text{then} \quad \mathbf{p}_M^{\Delta t} = \mathbf{D}_5 \mathbf{p}_M^0 + \mathbf{D}_6 \left( \mathbf{C}_s \dot{\mathbf{x}}^{\frac{\Delta t}{2}} + \mathbf{K}_s \mathbf{x}^{\frac{\Delta t}{2}} \right) + \mathbf{D}_7 \mathbf{p}_I^{\frac{\Delta t}{2}} \quad (3.35)$$

The displacements and pressures for subsequent time steps are calculated in a similar manner with the difference equations for the  $n^{\text{th}}$  time step reducing to

$$\begin{aligned} \ddot{\mathbf{x}}^{n\Delta t} &= -\mathbf{M}_s^{-1} \left( \mathbf{G} \mathbf{A}_f (\mathbf{p}_M^{n\Delta t} + (\mathbf{I} - \Gamma) \mathbf{p}_I^{n\Delta t}) \right) + \mathbf{C}_s \dot{\mathbf{x}}^{n\Delta t} + \mathbf{K}_s \mathbf{x}^{n\Delta t} \\ \dot{\mathbf{x}}^{\left(n+\frac{1}{2}\right)\Delta t} &= \dot{\mathbf{x}}^{\left(n-\frac{1}{2}\right)\Delta t} + \ddot{\mathbf{x}}^{n\Delta t} \Delta t \\ \mathbf{x}^{(n+1)\Delta t} &= \mathbf{x}^{n\Delta t} + \dot{\mathbf{x}}^{\left(n+\frac{1}{2}\right)\Delta t} \Delta t \\ \mathbf{x}^{\left(n+\frac{1}{2}\right)\Delta t} &= \frac{1}{2} \left( \mathbf{x}^{n\Delta t} + \mathbf{x}^{(n+1)\Delta t} \right) \\ \mathbf{p}_M^{(n+1)\Delta t} &= \mathbf{D}_5 \mathbf{p}_M^{n\Delta t} + \mathbf{D}_6 \left( \mathbf{C}_s \dot{\mathbf{x}}^{\left(n+\frac{1}{2}\right)\Delta t} + \mathbf{K}_s \mathbf{x}^{\left(n+\frac{1}{2}\right)\Delta t} \right) + \mathbf{D}_7 \mathbf{p}_I^{\left(n+\frac{1}{2}\right)\Delta t} \end{aligned} \quad (3.36)$$



## IV. CODE APPLICATIONS

### A. VERIFICATION EXAMPLES

In order to verify the accuracy of the finite element code, several example problems involving a wide variety of structural geometries and loadings are demonstrated. The exact analytical solutions are also presented for comparison when available.

#### 1. Free Vibration of a Dry, Isotropic Rod

Consider the transient response of an isotropic rod subjected only to an initial load which is released at time zero. One end of the rod is rigidly fixed while the other end is free as shown in Fig. 4.1. The finite element model was constructed with a uniform mesh of 20 brick elements laid end-to-end. For the case of a steel rod with length  $L=10$  ft, cross-sectional area  $A=1$  ft<sup>2</sup>, Young's modulus  $E=4.32 \times 10^9$  lb/ft<sup>2</sup>, density  $\rho=15.2$  slug/ft<sup>3</sup> and force  $F=1000$  lbs, the transient response is shown in Fig. 4.2.

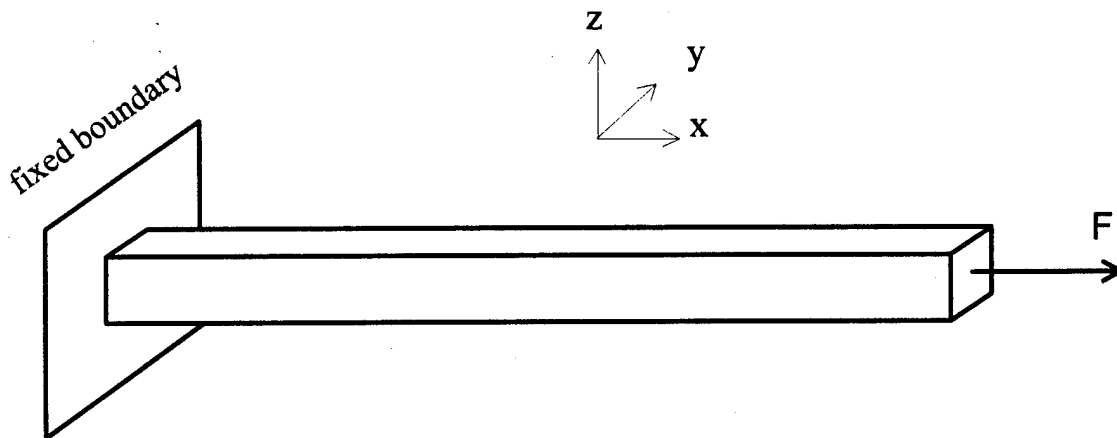


Figure 4.1. Dry Rod Problem Geometry

The analytical solution for the free response of a rod with a constant cross-sectional area and Young's modulus can be determined by the wave equation:

$$\frac{\partial^2 u}{\partial t^2} = c^2 \frac{\partial^2 u}{\partial x^2} \quad (4.1)$$

where  $u$  is the axial displacement at a point in the rod,  $c = \sqrt{\frac{E}{\rho}}$  is the speed of sound in the rod material. The solution to Eq. 4.1 is obtained by using the method of separation of variables with the result given by [Ref. 10]

$$u(x,t) = \frac{8FL}{\pi^2 AE} \sum_{n=0}^{\infty} \frac{(-1)^n}{(2n+1)^2} \sin \frac{(2n+1)\pi x}{2L} \cos \frac{(2n+1)\pi ct}{2L} \quad (4.2)$$

Substituting-in values for the current problem reduces Eq. 4.2 to

$$u(L,t) = 1.88 \times 10^{-6} \text{ ft} \sum_{n=0}^{\infty} \frac{(-1)^{2n}}{(2n+1)^2} \cos[(2n+1)2648t] \quad (4.3)$$

for displacement at the rod tip. The analytical solution including the first five terms in the series is also plotted in Fig. 4.2. Excellent agreement occurs between the FEM and analytical solutions.

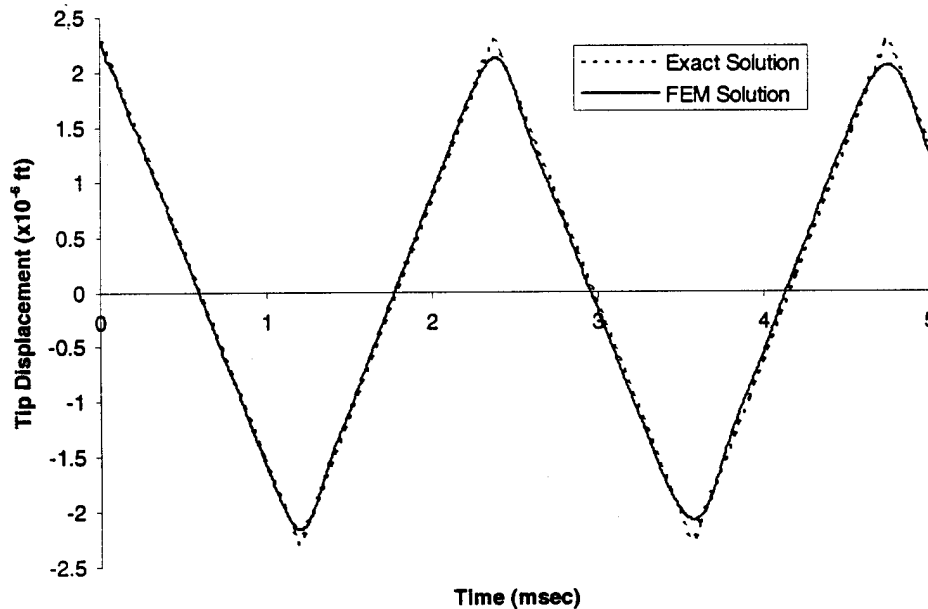


Figure 4.2. Dry Rod Transient Response



## 2. Dry, Isotropic Plate Subjected to a Step Pressure Loading

Now consider the dynamic response of a flat plate subjected to transverse loading such that plate bending occurs. A simply supported, isotropic, square plate subjected to a uniformly distributed step loading was modeled. For simplicity, only one-quarter of the plate was modeled with two sides simply supported and symmetric boundary conditions enforced on the remaining sides, as shown in Fig. 4.3. A 5 x 5 element mesh composed of nine-noded shell elements was used in the finite element solution. The transient response at the midpoint of a square aluminum plate with length  $a=5$  ft, thickness  $t=1$  in.,  $E=1.483 \times 10^9$  lb/ft<sup>2</sup> and  $\rho=5.25$  slug/ft<sup>3</sup> subjected to a 1 lb/ft<sup>2</sup> uniformly distributed step loading is shown in Fig. 4.4. Sinusoidal motion occurs with an amplitude of  $6.6 \times 10^{-5}$  ft. and a period of 18.6 msec.

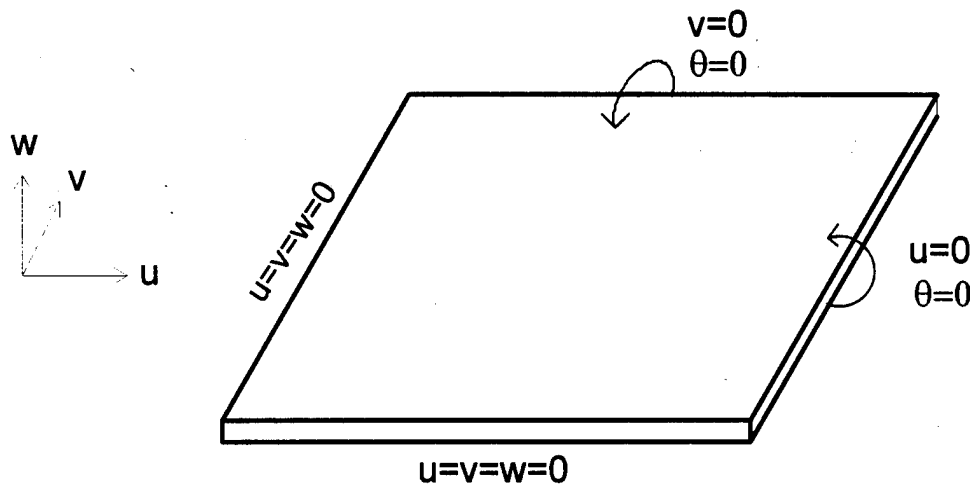


Figure 4.3. Dry Plate Problem Geometry

The analytical solution for the plate transient response can be obtained by examining both the plate static response and the undamped natural frequencies of vibration. For a simply-supported square plate subjected to a uniform load  $P_0$ , the static deflection at the midpoint is given by [Ref. 11]

$$w = \frac{16P_0}{\pi^6 D} \sum_{m=1,3}^{\infty} \sum_{n=1,3}^{\infty} \frac{(-1)^{\frac{m+n}{2}-1}}{mn \left[ \left( \frac{m}{a} \right)^2 + \left( \frac{n}{a} \right)^2 \right]^2} \quad (4.4)$$

$$\text{where } D = \frac{Et^3}{12(1-\nu^2)} \quad (4.5)$$

This series converges rapidly. If only the first four terms in the series are retained and  $\nu=0.3$ , then Eq. 4.4 can be simplified to

$$w = 0.0443 \frac{P_0 a^4}{Et^3} \quad (4.6)$$

Substituting in values for the current problem yields the static deflection at the plate midpoint of  $3.3 \times 10^{-5}$  ft. For a plate subjected to a uniform step loading, the plate midpoint deflection is expected to oscillate about the static deflection value with a maximum amplitude equal to twice the static deflection. This is exactly what occurs in the FEM solution.

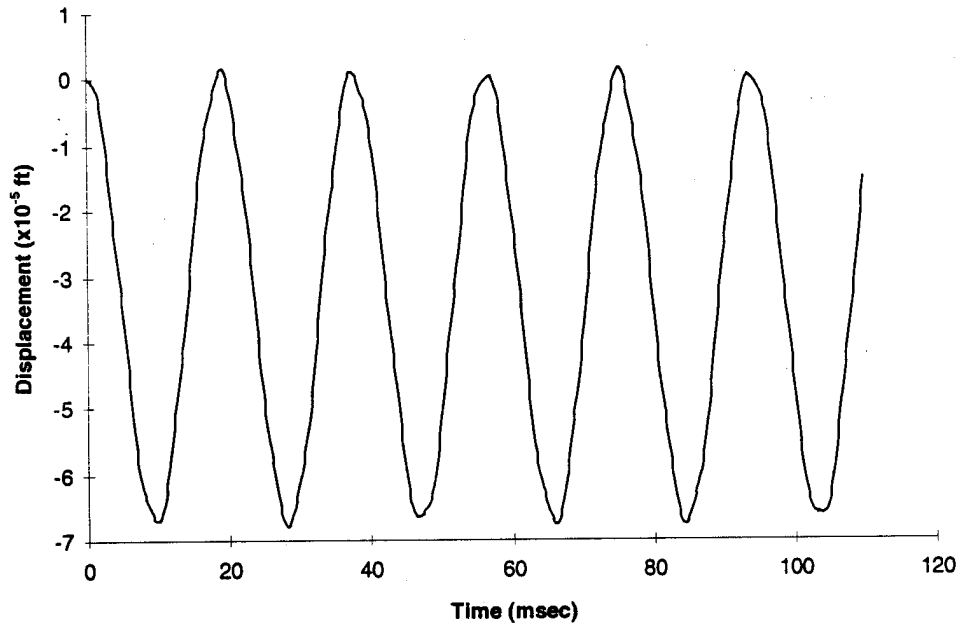


Figure 4.4. Dry Plate Transient Response

The undamped natural frequencies of an isotropic, simply supported square plate are given by [Ref. 12]

$$\omega_{m,n} = \left( \frac{\pi^4 D}{\rho t a^4} \right)^{\frac{1}{2}} (m^2 + n^2) \quad (4.7)$$

For a uniformly distributed step loading, the first mode of vibration is expected to be the dominant mode. Thus, setting  $m=n=1$  and substituting the constants for the current problem into Eq. 4.7 yields  $\omega_{11}=334.6$  rad/sec. This corresponds to a vibration period of 18.8 msec which is commensurate with the results shown in Fig. 4.4.

### 3. Wet, Isotropic Rod Subjected to a Step Pressure Loading

In order to assess the dynamic response of a submerged structure to an acoustic shock wave, consider a rod fixed at one end and subjected to a fluid pressure wave at the other end as shown in Fig. 4.5. Symmetric boundary conditions are imposed on the sides of the rod to produce a one-dimensional response along the longitudinal axis only.

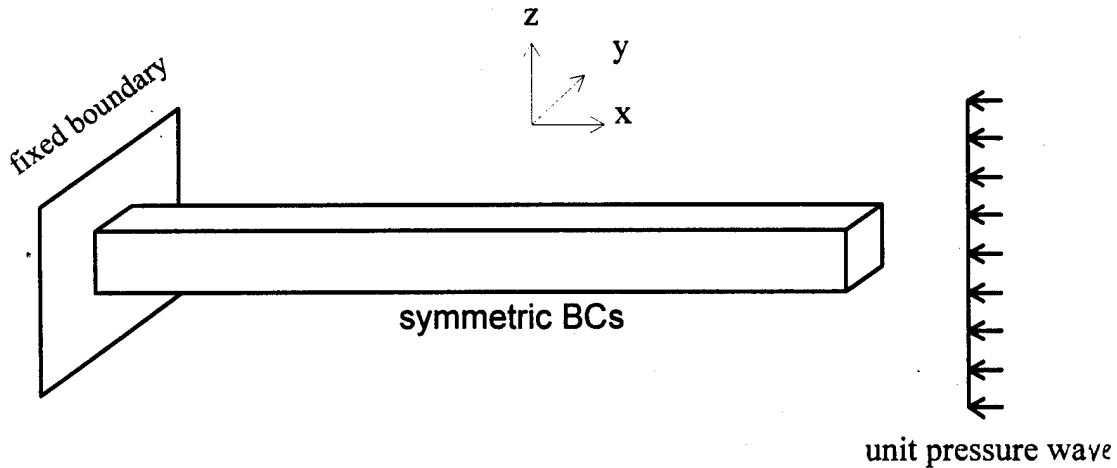


Figure 4.5. Wet Rod Problem Geometry

If the structure is homogeneous with a constant cross-sectional area, the incident pressure wave will propagate through the rod at the speed of sound for that material,  $c_0$ . This speed is related to the material density and elastic modulus by

$$c_0 = \sqrt{\frac{E}{\rho}} \quad (4.8)$$

When the pressure wave reaches the fixed boundary, it will be completely reflected as another compression wave of the same magnitude, causing the resultant stress at points immediately behind this reflected wave to be double the value of stress created by the original incident wave [Ref. 13]. Upon reaching the free edge, the wave will again be reflected. However, since the characteristic impedance,  $\rho c$ , of the fluid is much less than that of the structure, this reflected wave will be a tensile wave. If the surrounding fluid is air, whose impedance is negligible compared to that of the structure, then points in the structure immediately behind this reflected tensile wave will have a stress value equal to the incident wave pressure. When the tensile wave reaches the fixed boundary, it will be completely reflected as another tensile wave of the same magnitude. Thus points immediately behind this reflected tensile wave will have a zero-stress state. The theoretical stress response for a point at the midpoint of a 20 ft long aluminum rod in air subjected to a 1 lb/ft<sup>2</sup> incident wave is shown in Fig. 4.6.

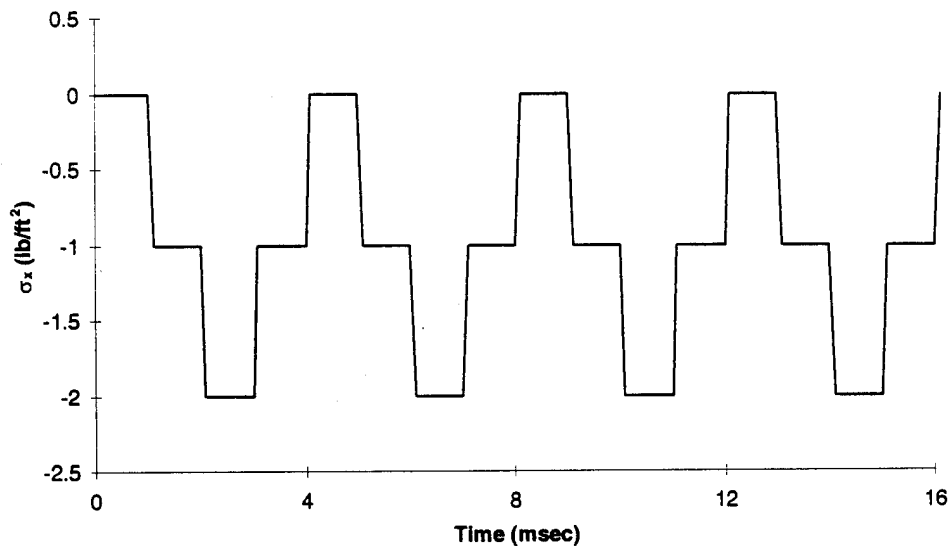


Figure 4.6. Theoretical Rod Midpoint Stress Response

If the rod is surrounded with water, then the structural dynamics is altered significantly. The impedance of water is 3600 times the impedance of air which allows the stress wave energy to be more readily transmitted into the fluid at the free end instead of being nearly completely reflected as was the case with air. This causes a dampening effect on the structural response. Figure 4.7 shows the finite element solution of the longitudinal normal stress time history at the midpoint of a 20 ft. long, aluminum rod impinged by a  $1 \text{ lb/ft}^2$  incident pressure wave with three different rod widths (square rod cross-section).

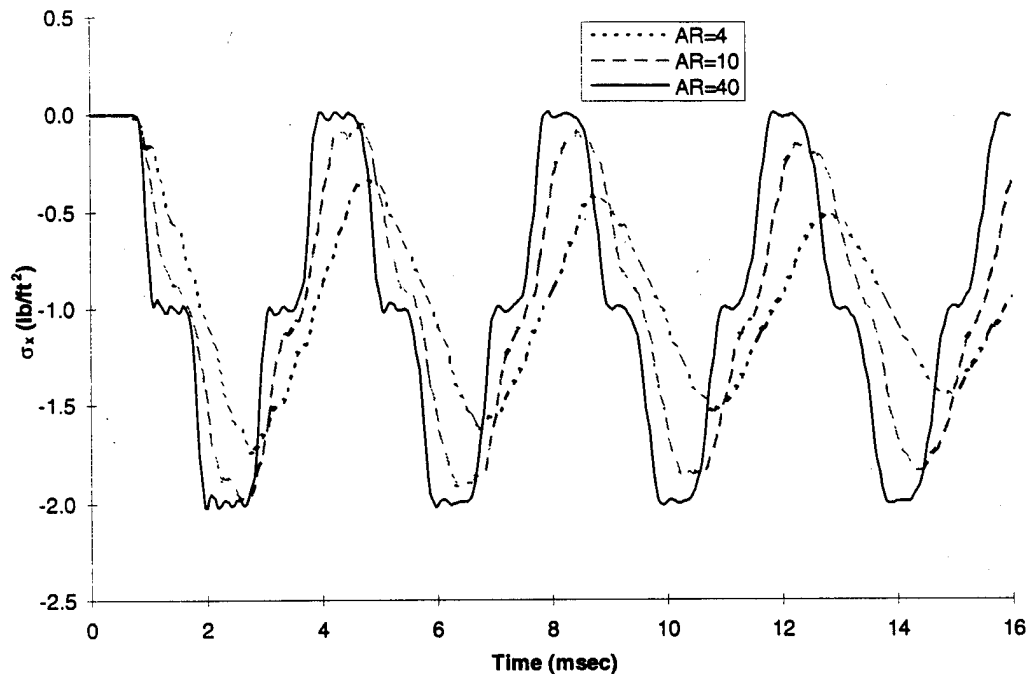


Figure 4.7. Wet Rod Longitudinal Stress History

The aspect ratio, AR, is defined as the rod length divided by rod width. As the cross-sectional area of the rod becomes larger while the rod length is held constant, the fluid dampening has a much greater effect causing the stress amplitude to decay faster over time. In addition, the added fluid mass becomes a larger fraction of the total system mass as the aspect ratio becomes smaller. This results in larger periods of oscillation with

smaller aspect ratios. For example, if the cross-sectional area of the rod is doubled while the rod length is held constant, then both the structural mass, wetted surface area, and structural stiffness in the longitudinal direction will double. However, the larger wetted surface can now entrain a deeper depth of fluid which causes the virtual fluid mass to more than double. Thus the total system mass grows faster than the stiffness as the aspect ratio is lowered causing the system frequency of oscillation to drop.

By contrast, the transient response of a rod in a vacuum subjected to a step load at the free end shows no dependence on the rod width as shown in Fig. 4.8. The rod geometry and material are identical to the wet rod examined above. In this case, if the rod width is doubled then both the total system mass and longitudinal stiffness double which produce no change in the undamped natural frequency. The dynamic response shown in Fig. 4.8 compares favorably to the theoretical response shown in Fig 4.6.

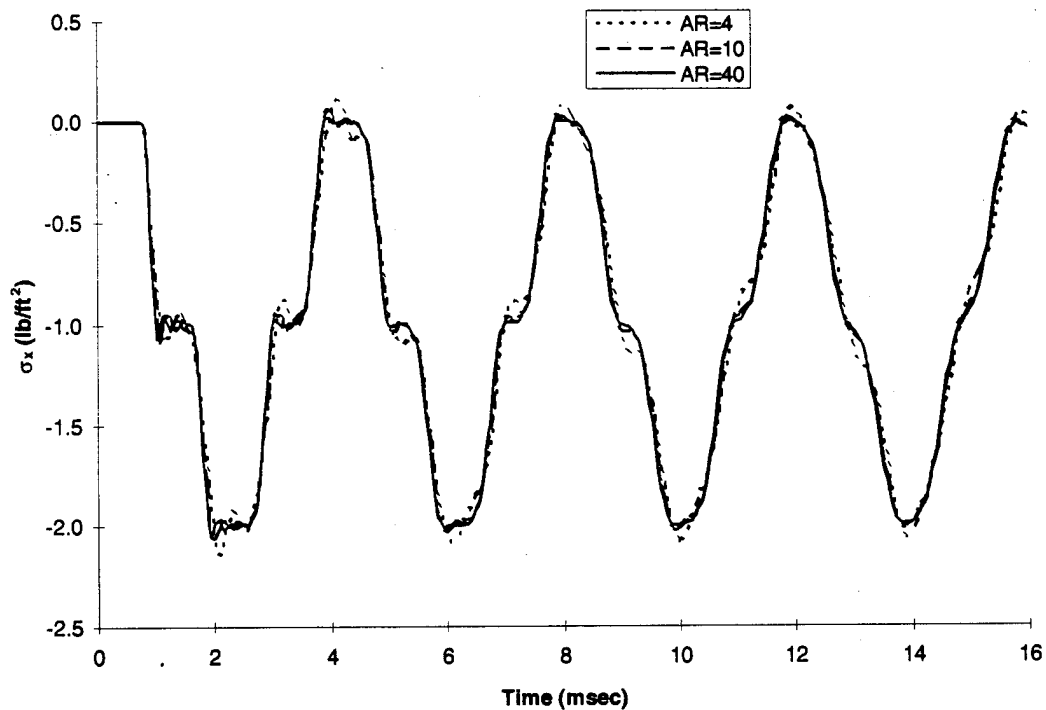


Figure 4.8. Dry Rod Longitudinal Stress History

#### 4. Wet, Isotropic Plate Subjected to a Step Pressure Loading

If the plate discussed in part IV.A.2 is submerged in water and subjected to a unit pressure wave, the displacement of the plate midpoint behaves as shown in Fig. 4.9. The maximum displacement is bounded by almost twice the static deflection shown in Fig. 4.4, but the response here is very highly damped. Furthermore, the period of oscillation for the wet plate is roughly three times the period of the dry plate due to the presence of the added fluid mass. As a matter of fact, the fluid mass contributes more to the total system mass than does the structural mass.

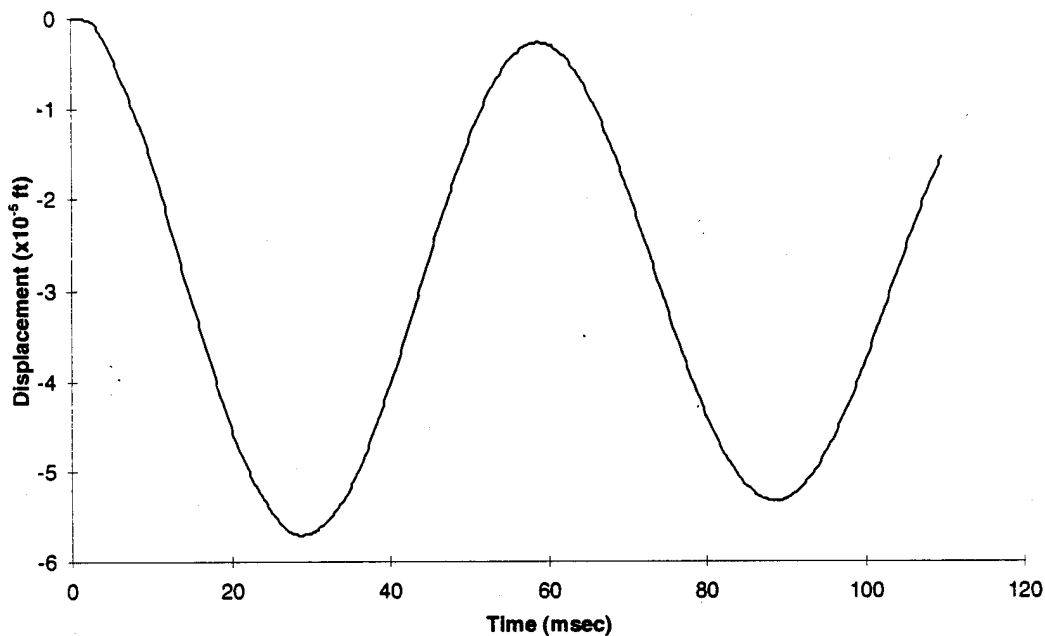


Figure 4.9. Wet Plate Midpoint Transient Response

The wet plate midpoint pressure component time histories are shown in Fig. 4.10. The total pressure is simply the sum of the incident and scattered pressure and is the actual pressure felt by a particle immediately behind the scattered wave. As can be seen, the total pressure oscillates about the incident wave magnitude with a period of

oscillation identical to that of the plate midpoint displacement response. The total pressure never drops below zero here because water cannot support a tension wave the way a solid material can.

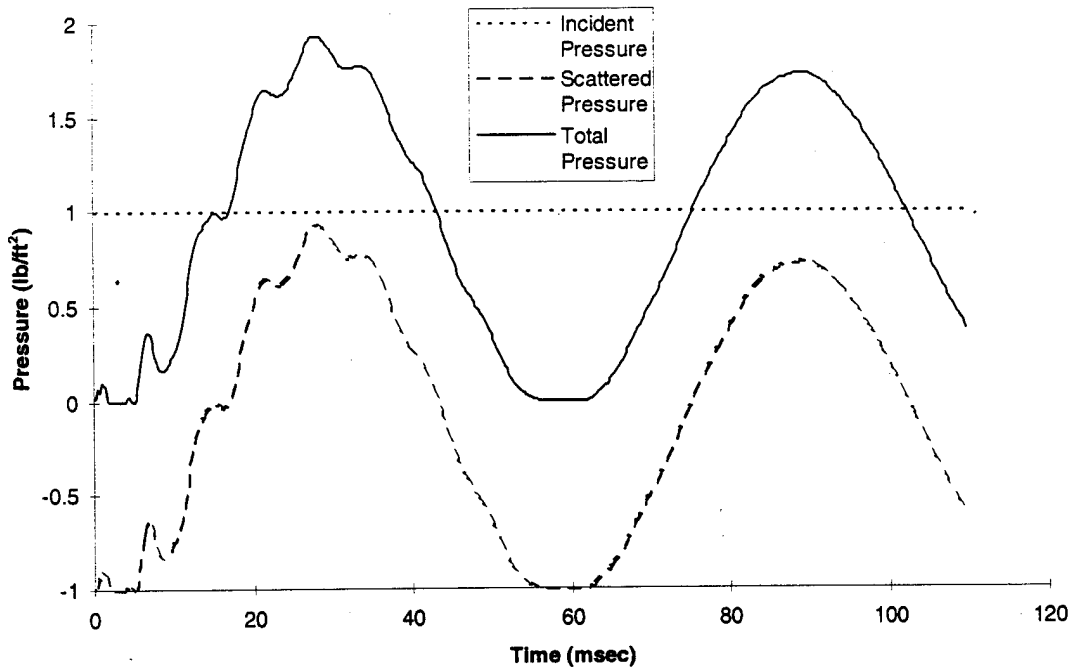


Figure 4.10. Wet Plate Fluid Pressure Response

## 5. Static Deflection of an Axisymmetric Cylinder

In order to verify the accuracy of finite element code when curved surfaces are encountered, consider the static response of a cylindrical shell clamped at one end and with a radial distributed load at the free end as shown in Fig. 4.11. Only one quarter of the cylinder was modeled due to symmetry considerations. The finite element formulation used 240 shell elements in a 10x24 mesh with a greater concentration of elements located near the free end where the displacement gradient was highest. The radial deflection is plotted in Fig. 4.12 along with the exact solution [Ref. 14]. Excellent agreement occurred between the two solutions.



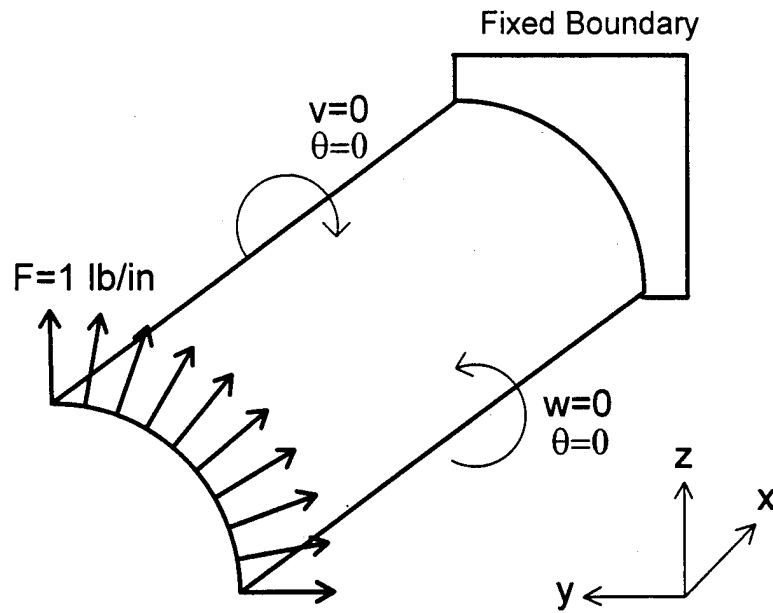


Figure 4.11. Axisymmetric Cylinder Problem Geometry

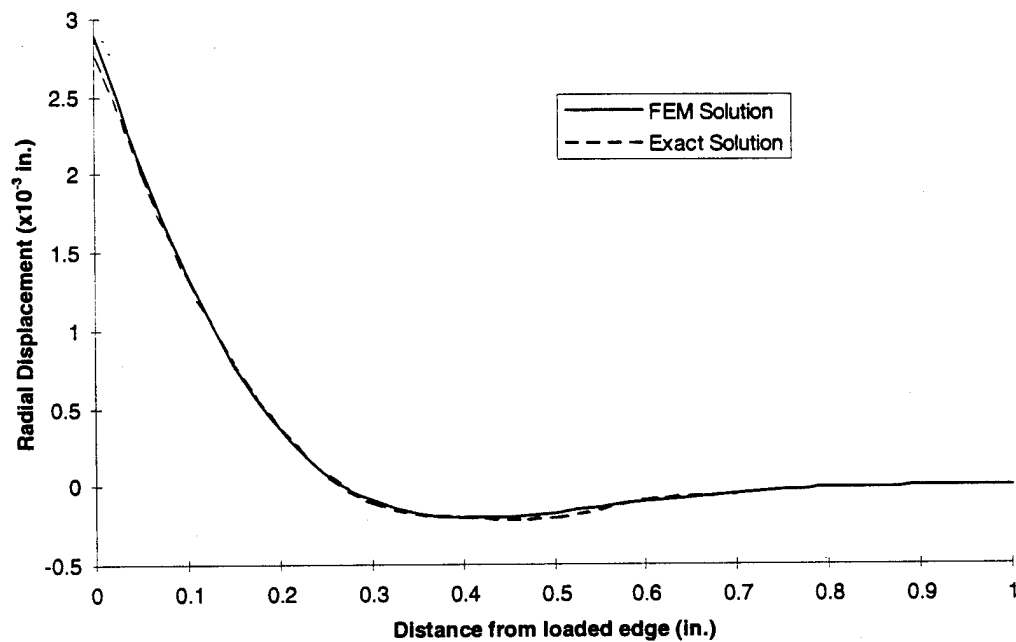


Figure 4.12. Radial Deflection of the Axisymmetric Cylinder

## 6. Static Deflection of an Angle-Ply Composite

To check the accuracy of the code when anisotropic material effects are included, consider the static response of a two-layer, square, antisymmetric  $(+\theta, -\theta)$ , angle-ply composite such as that shown in Fig. 4.13.

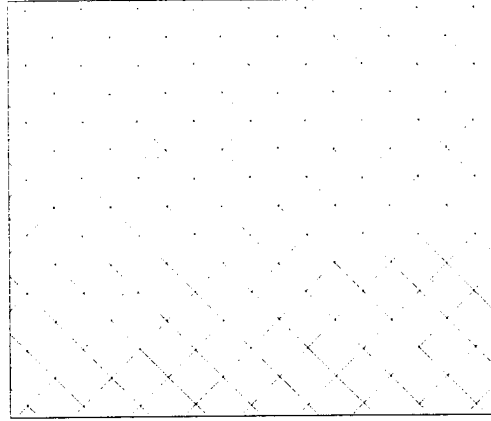


Figure 4.13. Angle Ply Composite

The composite is transversely loaded according to  $p = p_0 \sin \frac{\pi x}{a} \sin \frac{\pi y}{a}$  where  $a$  is the edge width. The material properties for each ply are as follows:

$$E_1/E_2=25, \quad G_{12}/E_2=0.6, \quad G_{22}/E_2=0.5, \quad \nu_{12}=0.25$$

When the finite element code was run on a one-quarter model using a  $5 \times 5$  shell element mesh with  $a=10$  ft.,  $E_1=2.5062 \times 10^9$  lb/ft<sup>2</sup>,  $p_0=100$  lb/ft<sup>2</sup>,  $h=a/6$  and various ply angles, the normalized midpoint deflections were as shown in Fig. 4.14. The published solution was also obtained numerically [Ref. 15]. The error between the two solutions is mainly attributed to lumping the load distribution over each element at the central element node in the present formulation. This force lumping method was used because the same computer code was used to solve fluid-structure interaction problems and with those type of problems, only one element nodal point is available to apply the pressure loading. If a truly consistent force vector was used for this dry, composite problem, then slightly better results would be expected.

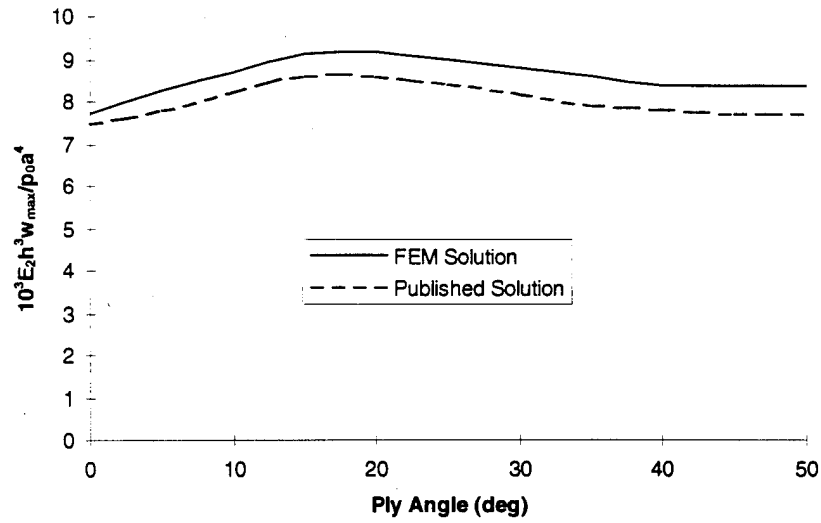


Figure 4.14. Midpoint Deflection for a Two Layer Angle-ply Composite

### 7. Wet, Isotropic Sphere Subjected to a Step Pressure Loading

The last verification example examines the dynamic response of a submerged, unrestrained, spherical shell to an incident plane wave as shown in Fig. 4.15.

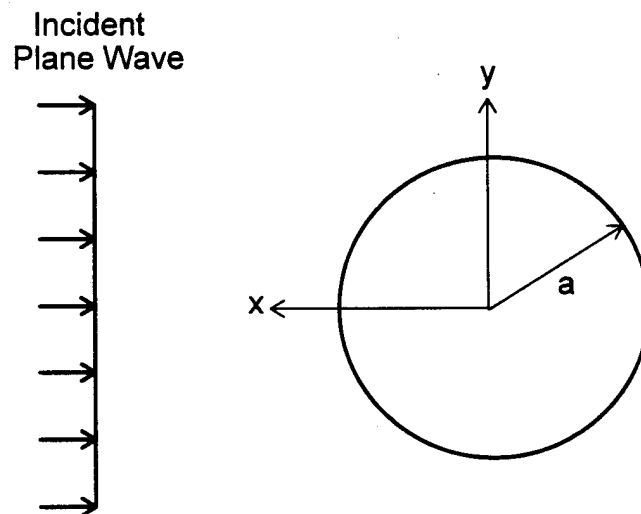


Figure 4.15. Spherical Shell Problem Geometry

The finite element formulation uses an upper-half model consisting of 24 shell elements arranged in a hemisphere with symmetric boundary conditions applied along the equator. The sphere has a radius  $a=1.0$  m and thickness  $b=0.02$  m. The sphere is made of steel with properties  $E=206.84$  GPa,  $\nu=0.33$ ,  $\rho=7784.5$  kg/m<sup>3</sup> and the surrounding water has sound speed  $c=1461.2$  m/s and density  $\rho=999.6$  kg/m<sup>3</sup>. The incident wave of pressure  $1.0$  N/m<sup>2</sup> is modeled as a spherical wave with a very large standoff distance in order to approximate a plane wave. The normalized velocity response of the points on the sphere closest and farthest from the charge are shown Fig. 4.16 and Fig. 4.17, respectively. The analytical solution was obtained using the the method of separation of variables [Ref. 19] and is shown for comparison. A numerical solution obtained with the USA/DYNA3D software combination [Ref 20] is also shown. Since the USA/DYNA3D software uses the more exact DAA2 doubly asymptotic approximation which includes the effects of curvature in the fluid mass matrix construction, it is expected to yield slightly better results than the present formulation which is based on the simpler DAA1 method. However, the present method tracks reasonably well with the analytic solution for the early time response.

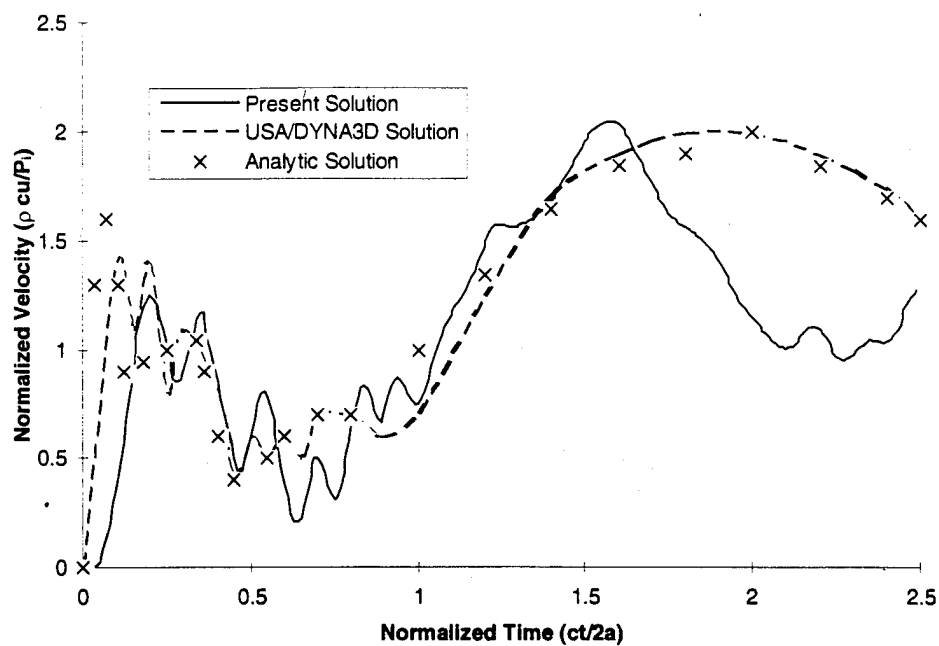


Figure 4.16. Near Element Response

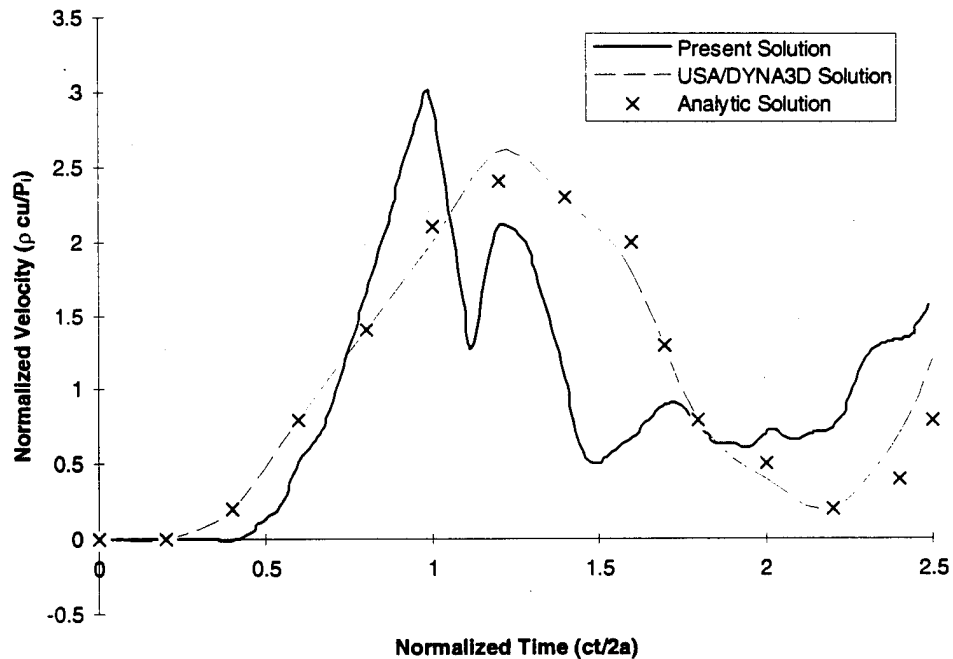


Figure 4.17. Far Element Response

## B. UNBALANCED SANDWICH COMPOSITE IMPACT STUDY

Sandwich composites are becoming increasingly more popular as structural components for military applications. These composites are constructed of two strong facesheets separated by a thick, lightweight, weaker core. The resulting composite can have a much higher specific strength than a comparable monolithic material. One application of this composite of interest to the Navy is its use in the Advanced Performance Mast System (APMS). This particular sandwich composite has titanium and glass fiber reinforced plastic (GRP) facesheets separated by a phenolic, Nomex fiber reinforced honeycomb core. Since the facesheets are of different material, this type of sandwich composite is termed "unbalanced."

The objectives of this study are to generate a numerical model of the unbalanced sandwich composite and then use this model to simulate the dynamic response of the composite subject to impact loading, with and without material failure.

An experimental impact study was conducted by Fuller [Ref. 7] on samples of the unbalanced sandwich composite used on the APMS. The samples had length = 12.0 in., width = 2.75 in. and a nominal thickness of 1.18 in. The three-point impact tests used a fixture which held the composite beams in a simply supported configuration with the impactor striking the center of the beam as shown in Fig. 4.18. The supports were located 0.5 in. from each end. Five strain gages were bonded to the beam as shown in Fig. 4.19.

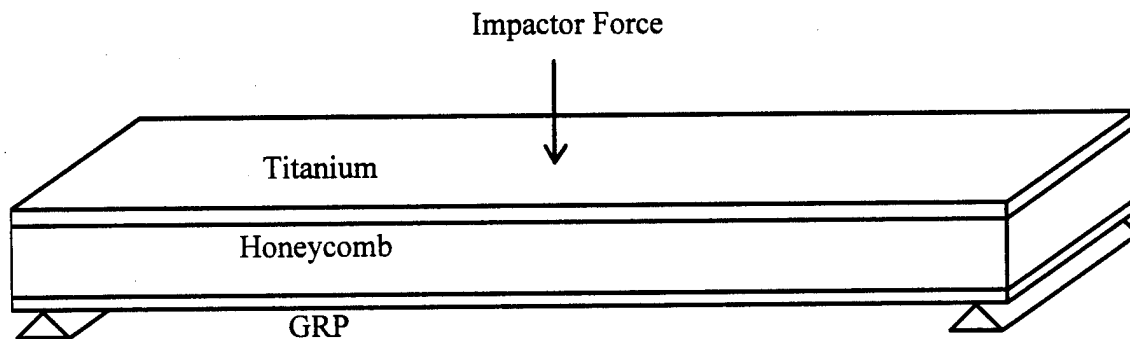


Figure 4.18. Unbalanced Sandwich Composite

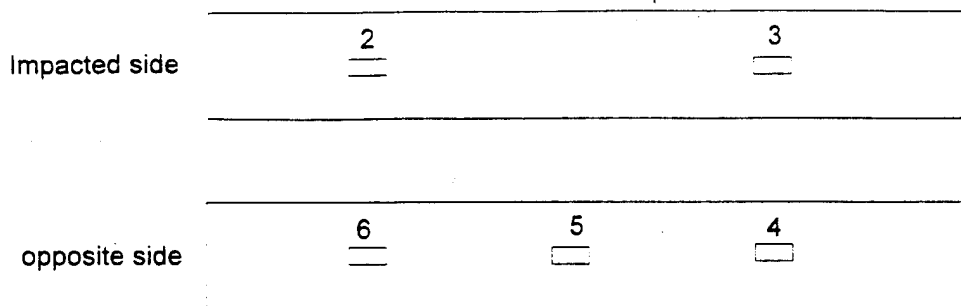


Figure 4.19. Strain Gage Placement

Strain gage #5 was located at the center of the beam on the opposite side of the impact with the remaining strain gages located at the beam quarter points.

The first test to be modeled is the impact of a 125 lb. mass dropped from a height of 1.0 in. (0.0254 m.) onto the midpoint of the sandwich composite. This drop height was small enough that material failure did not occur. The experimental test used a force transducer located between the beam and impactor to measure the impact force throughout the impact process. Fig. 4.20 shows the impact force time history which was

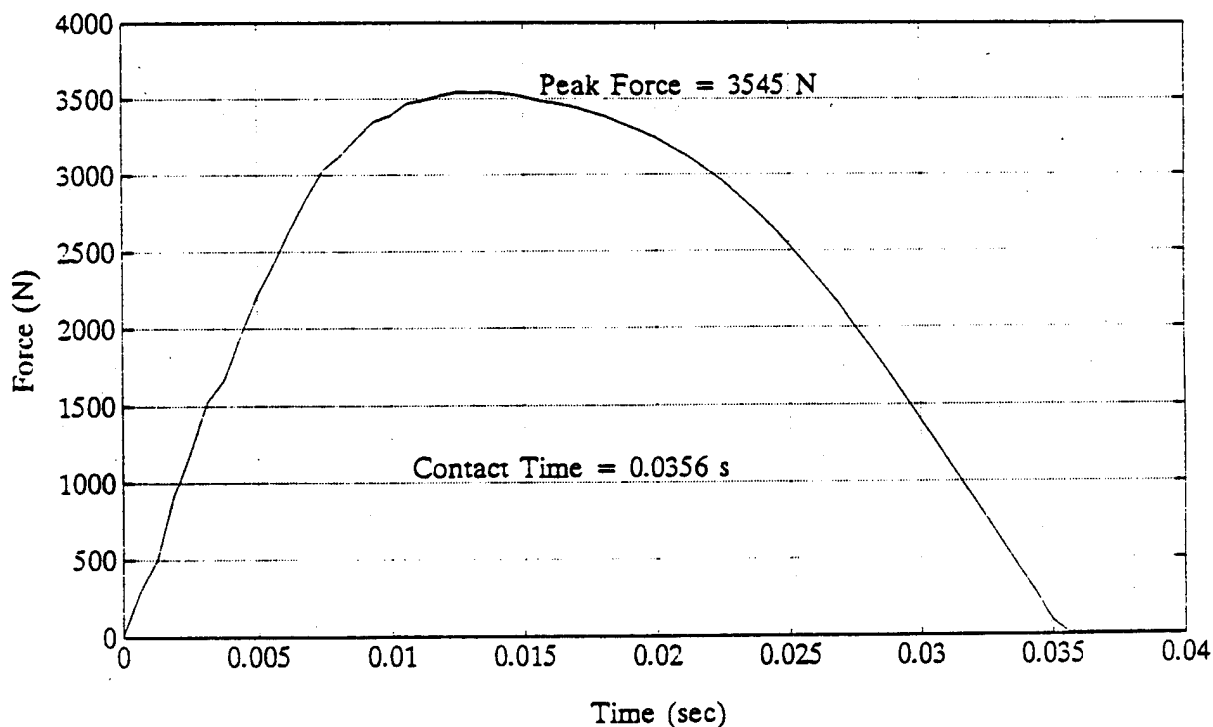


Figure 4.20. Experimental Impact Force Time History for 1.0 in. Drop

used as an input to the finite element code. In the experimental setup, a thin strip of brass was fastened to the center of the beam to spread out the contact load over the width of the beam. This was modeled in the finite element formulation by treating the impact load as a line force across the width of the beam.

The finite element model of the sandwich composite was constructed with 12 nine-noded shell elements of equal length laid end-to-end. Each element consisted of three layers stacked on top of each other with different material properties in each layer. Table 4.1 summarizes the material properties for each layer.

	Titanium	Honeycomb	GRP
$E_{11}$ (psi)	$15.5 \times 10^6$	$28.0 \times 10^3$	$2.5 \times 10^6$
$E_{22}$ (psi)	$15.5 \times 10^6$	$28.0 \times 10^3$	$2.5 \times 10^6$
$G_{12}$ (psi)	$5.77 \times 10^6$	$9.5 \times 10^3$	$1.2 \times 10^6$
$G_{13}$ (psi)	$5.77 \times 10^6$	$4.7 \times 10^3$	$4.48 \times 10^5$
$G_{23}$ (psi)	$5.77 \times 10^6$	$4.7 \times 10^3$	$4.48 \times 10^5$
$\nu_{12}$	0.342	0.47	0.33
$\rho$ (slug/ft <sup>3</sup> )	9.18	0.1245	3.69
Nominal thickness (in.)	0.1	1.0	0.08
Actual thickness (in.)	0.106	1.0	0.083

Table 4.1. Sandwich Composite Material Properties

The experimental strain gage readings for the first impact test are shown in Fig. 4.21 while the numerical simulation results are shown in Fig. 4.22. Since the beam is symmetric and no failure occurs, the strain histories for strain gages #4 & #6 are identical as are the strains for gages #2 & #3. The numerical simulation tracks reasonably well with the experimental results for strain gages #2 & #3 which are located on the top of the composite and undergo compression. However, the numerical simulation differs from the experimental results for the strain gages located on the beam bottom. If we assume that the beam behaves according to linear elastic beam theory and neglect the shear deformation, then the strain at the midpoint of the beam (gage #5) should always be a



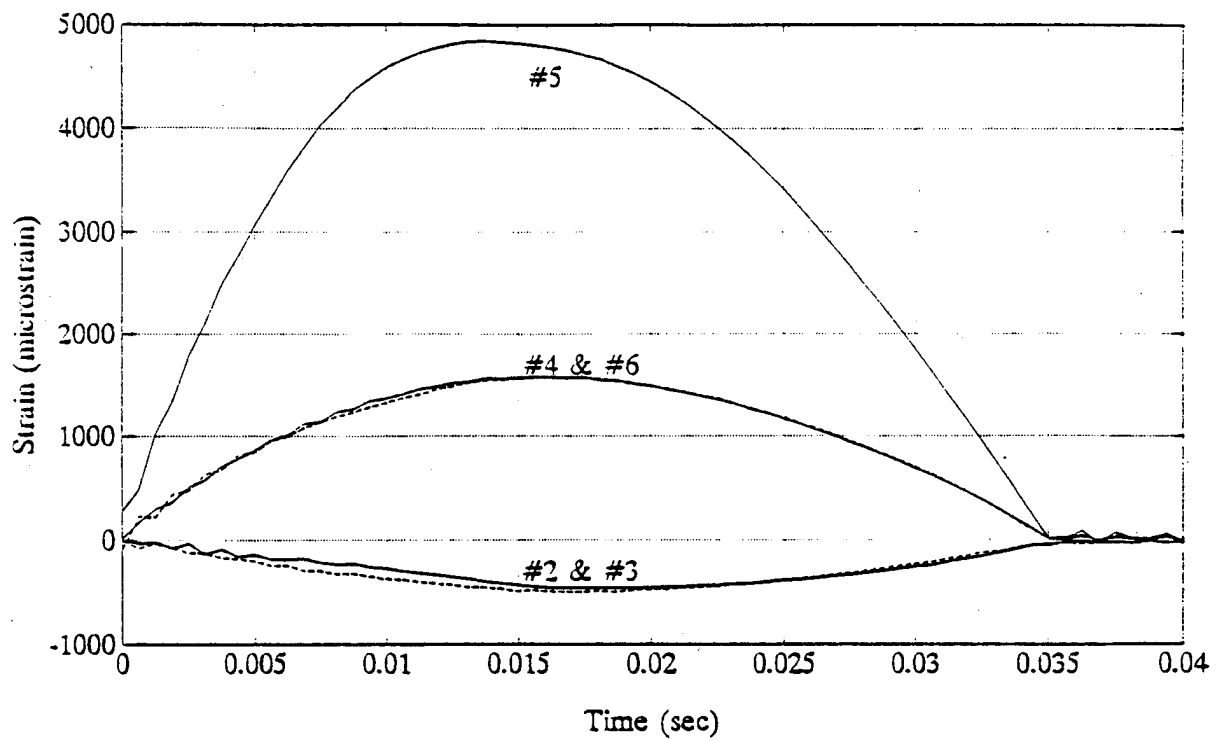


Figure 4.21. Experimental Results of The Impact Test with Drop Height = 1.0 in.

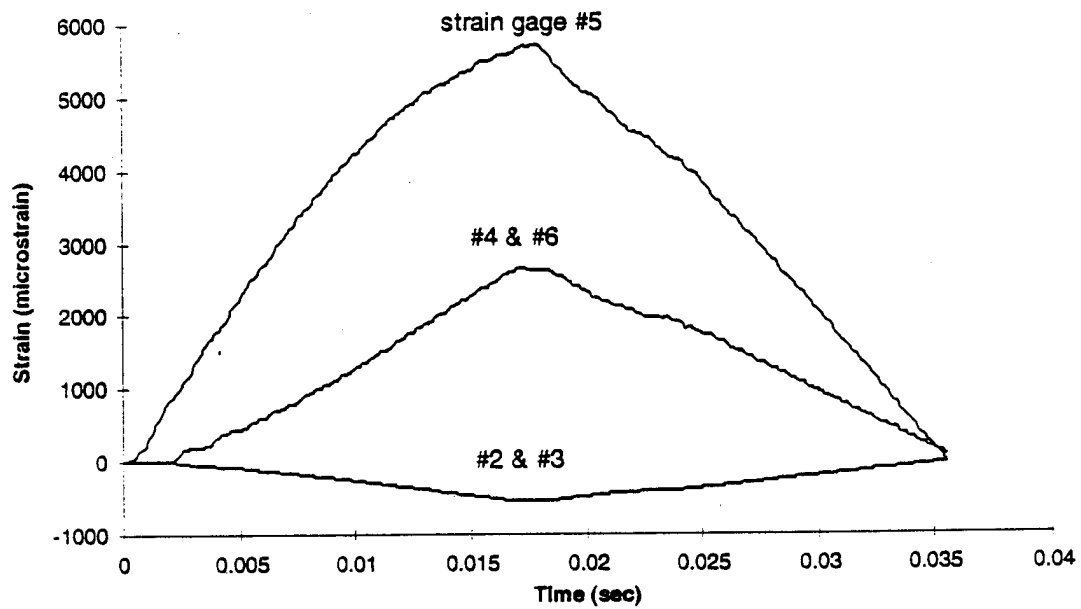


Figure 4.22. Numerical Simulation of the Impact Test with Drop Height = 1.0 in.

factor of 2.2 greater than the strain at the beam quarterpoints (#4 & #6). This factor of 2.2 accounts for the supports not being located exactly at the beam ends. If the supports were exactly at the beam ends then the factor would be 2.0 as expected. The numerical simulation, which is based on linear elastic theory, does indeed show the strain at the beam midpoint to be approximately a factor of 2.2 higher than the strains at the quarterpoints. By contrast, the experimental test shows the midpoint strain to be roughly a factor of 3.1 times the quarterpoint strains. This disparity cannot be accounted for by the presence of the shear deformation alone. Thus, although the numerical simulation can reasonably predict the sandwich composite response using linear elastic theory, some nonlinear effects are clearly present in the actual dynamics of the sandwich composite and need to be appropriately modeled.

The next experimental test to be simulated uses the same material and setup as the previous case but with an impactor drop height of 1.5 in. This height is large enough to cause a partial failure of the sandwich composite material. The experimentally determined impact force time history is shown in Fig. 4.23. The sharp drop in the impact force at time 0.01 seconds is due to the composite suddenly relaxing due to partial material failure.

The experimental strain gage readings for the second impact test are shown in Fig. 4.24 while the numerical simulation results are shown in Fig. 4.25. The strains in both the experimental test and simulation up to the time of failure follow the same trends as they did for the impact test with a drop height of 1.0 in. At time 0.01 seconds, the sudden drop in the impact force tends to cause the strain at all points in the beam to decrease. This can be seen in Fig. 4.24 for strain gages #3, #4 & #6. However, material failure occurs at the beam quarterpoint where strain gages #2 & #6 are located. This causes the material to relax at that point which tends to cause a large increase in tensile strain for strain gage #6 and a large increase in compressive strain for strain gage #2. The increase in strain at the quarterpoint due to material failure is much more significant than the decrease in strain at the quarterpoint due to the lower impactor force. The end result is that the strain increases sharply at the beam quarterpoint at the time of failure.

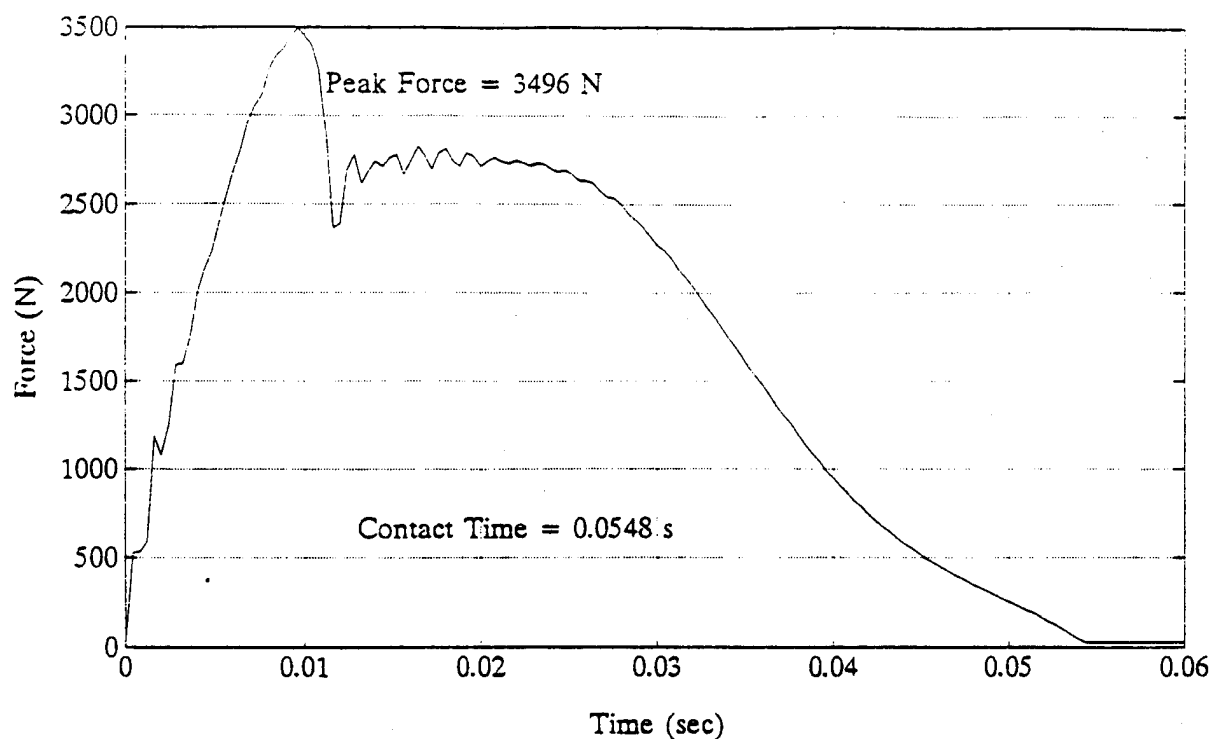


Figure 4.23. Experimental Impact Force Time History for 1.5 in. Drop

In order to simulate failure in the finite element analysis of the sandwich composite, the modulus of elasticity of each layer for the two elements bordering the beam quarter point was reduced by 40% at the time of failure. The global stiffness matrix was then regenerated and the transient analysis continued. As can be seen in Fig. 4.25, the strain response can be reasonably predicted using this method. An alternate method to simulate failure would be to reduce the effective load carrying thickness of a particular layer where failure initiates. Although these methods may seem somewhat arbitrary in their approach to fracture, the purpose of this study was to observe the effects of fracture on the dynamic response of the composite. Further research needs to be devoted to determine how failure initiating in the core material weakens the structure on a global scale to produce the results seen in the experimental study.

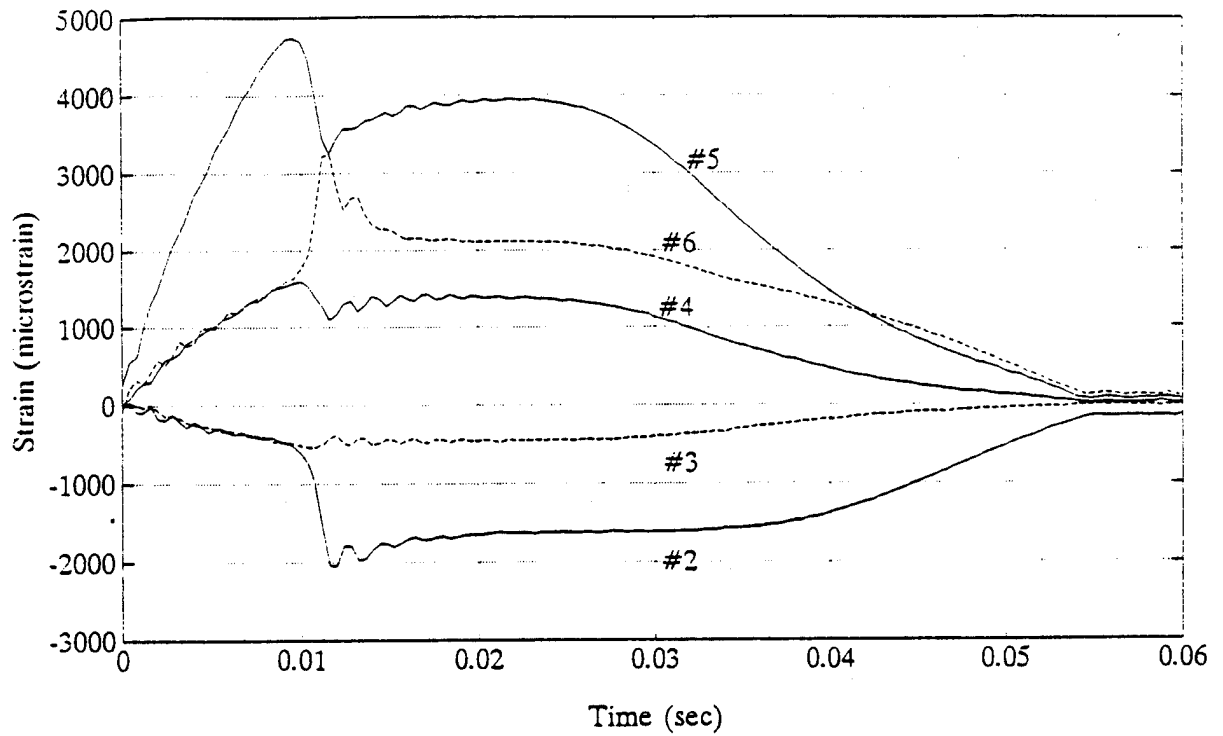


Figure 4.24. Experimental Results of the Impact Test with Drop Height = 1.5 in.

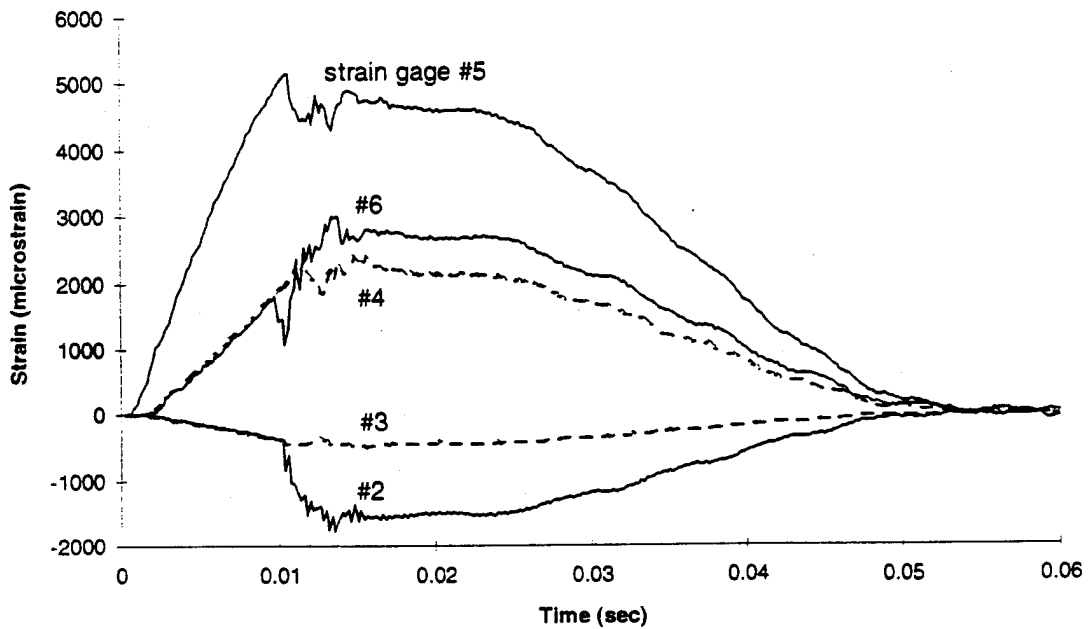


Figure 4.25. Numerical Simulation of the Impact Test with Drop Height = 1.5 in.

### C. EFFECTS OF COMPOSITE LAYER SMEARING ON THE FLUID-STRUCTURE INTERACTION

When the number of layers in a composite laminate becomes large, the computer time required to generate the structural stiffness matrix can become prohibitively expensive. A method which combines the material properties of several adjacent composite laminae into an single layer of equivalent stiffness, termed "smearing", is demonstrated below for structures excited by underwater shock.

Consider a filament wound S-glass/epoxy composite with ten equally thick layers layed-up as follows: [0/45/90/-45/90/45/90/-45/90/90]. This fiber orientation, as studied by Rousseau [Ref. 21], is intentionally non-symmetrical with respect to the midplane. The conventional method to generate an element stiffness matrix of this composite would be to first determine the constitutive relations matrix,  $\mathbf{D}_{\text{ortho}}$ , for each layer in its associated material (1,2,3) coordinate system (see Fig. 2.2). This matrix is then transformed into global coordinates to become  $\mathbf{D}_{\text{shell}}$  and used along with the strain-displacement matrix,  $\mathbf{B}_{\text{shell}}$ , to determine the layer stiffness. The stiffness of each layer is then added to generate the element stiffness matrix for the composite.

The method used here to reduce the computational time required to generate the stiffness matrix involves conducting a weighted average of the constitutive matrix for each layer,  $\mathbf{D}_{\text{ortho, layer}}$  to arrive at the smeared constitutive matrix,  $\mathbf{D}_{\text{ortho, smeared}}$ , according to

$$\mathbf{D}_{\text{ortho, smeared}} = \frac{\sum_{i=1}^n h_i \mathbf{D}_{\text{ortho, layer}_i}}{\sum_{i=1}^n h_i} \quad (4.9)$$

where  $n$  is the number of layers and  $h_i$  is the thickness of  $i^{\text{th}}$  layer. For example, if it is desired to smear all ten layers of the composite mentioned above into one layer, the smeared constitutive matrix would be calculated by

$$\mathbf{D}_{\text{ortho, smeared}} = \frac{1}{10} (\mathbf{D}_0 + 5\mathbf{D}_{90} + 2\mathbf{D}_{45} + 2\mathbf{D}_{-45}) \quad (4.10)$$

This smeared constitutive matrix needs to be calculated only once for the structure, assuming the layer thicknesses and material characteristics do not change from one element to the next. The effective material constants for this smeared layer can also be generated from the smeared constitutive matrix, if desired for comparison purposes, but this is not required to implement the smearing formulation.

To illustrate this smearing process in a fluid-structure interaction problem, consider a simply supported plate, 5.0 ft. on each side and is 1.0 in. thick, fabricated with the ten layer composite material discussed above. The plate is exposed to water on one face and is excited by a  $1000 \text{ lb/ft}^2$  plane incident wave. The plate midpoint transverse deflection time history is shown in Fig. 4.26 and the midpoint wet surface pressure time history is shown in Fig. 4.27 for various smearing scenarios.

The first case is the baseline transient response with all composite layers used to calculate the stiffness matrix in the conventional manner. The next case smears all ten layers into one effective layer. This results in a poor approximation to the unsmeared model as the peak midpoint displacement undershoots by 11% and the peak displacement is also significantly displaced toward an earlier time. The peak surface pressure and time to peak pressure are not altered significantly, however. The third case uses three layers in a 0 / smear / 90 orientation where the smeared layer consists of the eight central plies of the original ten layer laminate. Much more satisfactory results occur with this case as the peak midpoint deflection undershoots by only 3.5% compared to the unsmeared model. In addition, the midpoint surface pressure response is nearly identical to the unsmeared case. The last case uses five layers in a 0 / 45/ smear / 90 / 90 orientation where the smeared layer consists of the six central plies of the original ten layer. Little is gained using five layers instead of only three layers as the peak displacement overshoots by only 3.3% and the surface pressure history is again nearly identical to the unsmeared model. Note - since the 10 layer composite we have been using here as an example contains two 45 / 90/ -45 groups, it behaves as a quasi-isotropic material. If another composite layer orientation had been selected which gave a much greater preference to one direction only, then the results discussed above would be even more pronounced.

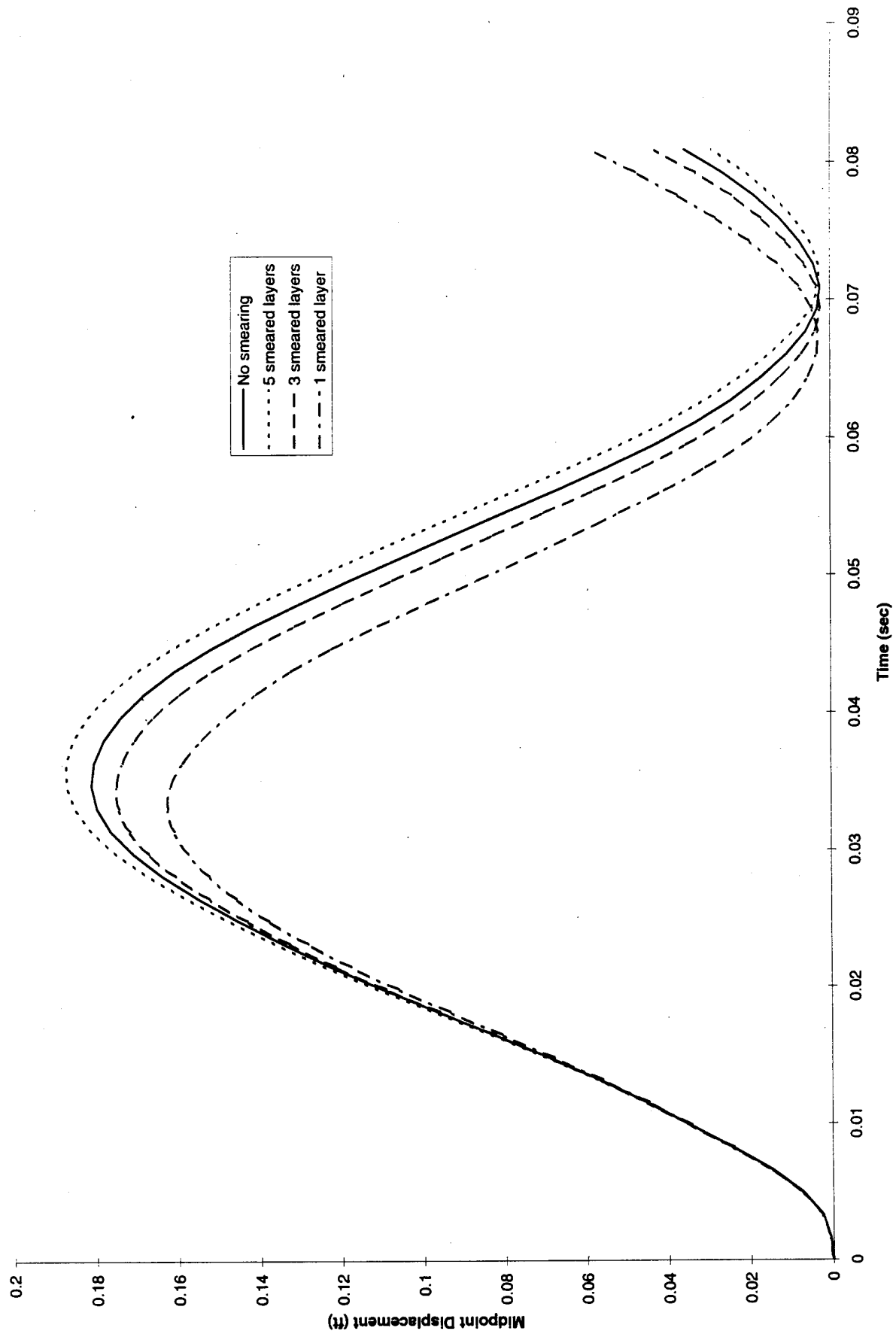


Figure 4.26. Composite Plate Midpoint Deflection Response

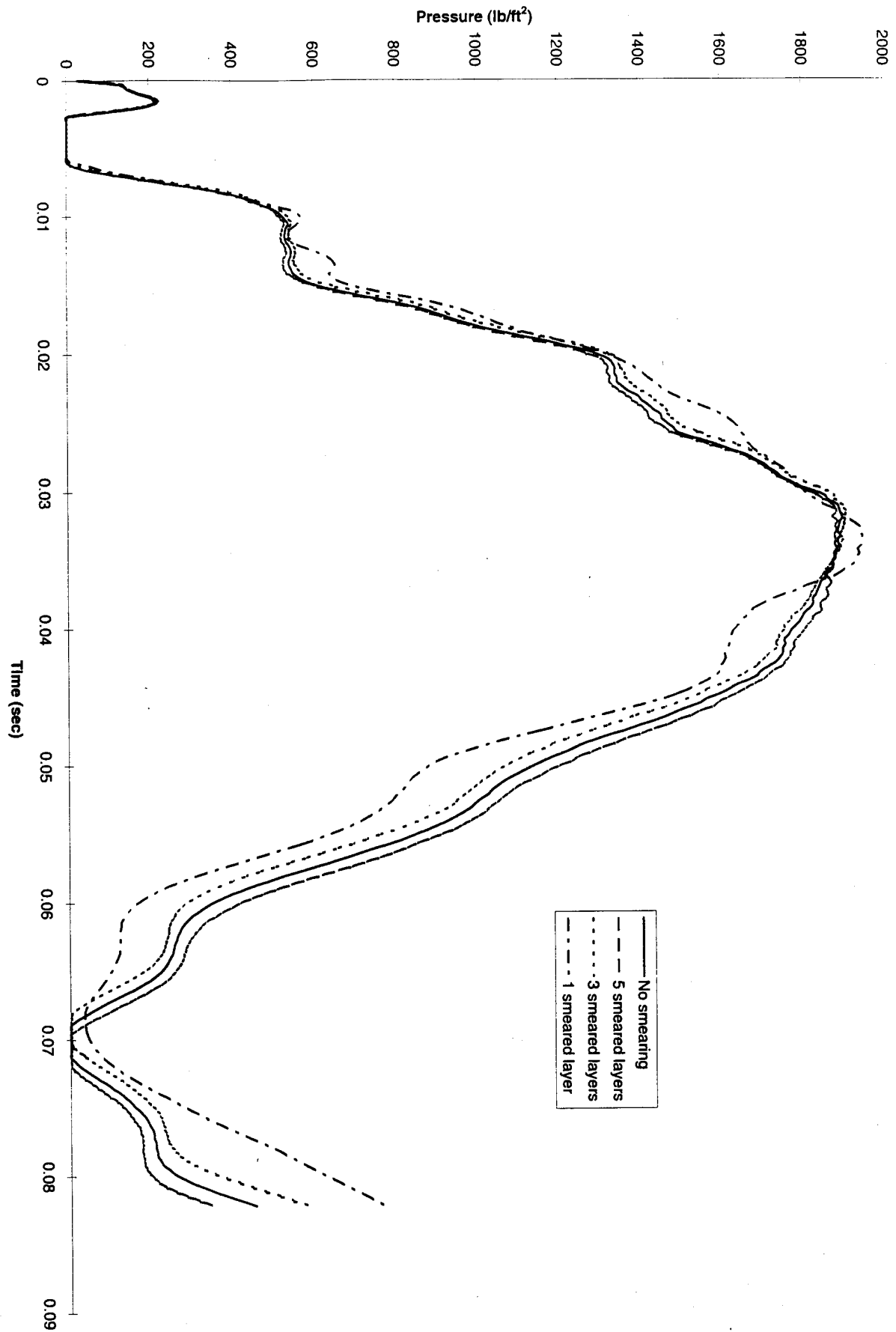


Figure 4.27. Composite Plate Midpoint Surface Pressure Response



Since the outer layers carry most of the load in thin composite structures subjected to transverse loading from the fluid-structure interaction, any attempts to include these layers in the smearing process is not recommended. On-the-other-hand, composite layers near the midplane contribute little to the bending stiffness so they are the best candidates for smearing, as was shown in Figs. 4.26 and 4.27.



## V. CONCLUSION

The general purpose finite element/boundary element code developed here has been shown to be useful in simulating fluid-structure interaction and impact problems. Although only linear elastic effects have been incorporated at this point, it can be readily tailored to solve specific problems such as those dealing with modern composite materials. With further refinement, it will prove to be a valuable tool in future underwater shock research.

The following items are recommended to be incorporated into future revisions of the code to improve its accuracy and scope:

1. Include higher order methods to solve the integrals of Eqs. 3.11 and 3.12 in the generation of the fluid mass matrix as discussed in Ref. 4. These more advanced methods provide better results with coarse meshes and handle local curvature effects more accurately.
2. Utilize the second Doubly Asymptotic Approximation,  $DAA_2$  [Ref. 3], in the governing equations for the fluid-structure interaction. This method is a generalization of the  $DAA_1$  to a symmetric second order differential equation with improved accuracy in the intermediate frequency range. It can better handle global curvature of the submerged structure.
3. Implement the Kwon micromechanical model [Refs. 22-24] to determine the micro-level fiber and matrix stresses. These stresses can be used in a stiffness reduction correlations to better estimate material property degradation and to model damage progression until material failure.



## LIST OF REFERENCES

1. Bathe, K., *Finite Element Procedures on Engineering Analysis*, Prentice-Hall, Inc., Englewood Cliffs, pp. 144-145, pp. 194-297, 1982.
2. Vinson, J. R. and Chou, T., *Composite Materials and their Use in Structures*, John Wiley & Sons, Inc., New York, pp. 201-223, 1975.
3. DeRuntz, J. A., "The Underwater Shock Analysis Code and its Applications," *60th Shock and Vibration Symposium Proceedings*, Vol. I, pp. 89-107, David Taylor Research Center, Nov., 1989.
4. DeRuntz, J. A. and Geers, T. L., "Added Mass Computation by the Boundary Integral Method," *International Journal for Numerical Methods in Engineering*, Vol 12, 1978, pp. 531-550.
5. Huang, H., Everstine, C. C. and Wang, Y. F., "Retarded Potential for Analysis of Submerged Structures Impinged by Weak Shock Waves," *Computational Methods for Fluid-Structure Interaction Problems*, AMD-Vol 26, American Society of Mechanical Engineers, December 1977.
6. Brasek, T. P., (1994) *Response of Dual-Layered Structures Subjected to Shock Pressure Wave*, Master's Thesis, Naval Postgraduate School, Monterey, California.
7. Fuller, L. B., (1994) *Damage and Compressive Failure of Unbalanced Sandwich Composite Panels Subject to a Low-Velocity Impact*, Master's Thesis, Naval Postgraduate School, Monterey, California.
8. Chiong, L. N., (1994) *Study of Air-Backed and Water-Backed Composite Cylinders Subjected to Underwater Explosion*, Master's Thesis, Naval Postgraduate School, Monterey, California.
9. Akin, J. E., *Finite Elements for Analysis and Design*, Academic Press, pp. 359-421, 1994.
10. Haberman, R., *Elementary Applied Partial Differential Equations*, 2<sup>nd</sup> Edition, Prentice-Hall, Inc., pp. 113-124, 1987.
11. Ugural, A. C. and Fenster, S. K., *Advanced Strength and Applied Elasticity*, 2<sup>nd</sup> Edition, Prentice-Hall, Englewood Cliffs, pp. 419-421, 1987.
12. Timoshenko, S., *Theory of Plates and Shells*, McGraw Hill, New York, 1959.

13. Kolsky, H., Stress Waves in Solids, New York, Dover Publications, Inc., 1963.
14. Zienkiewicz, O. C., The Finite Element Method, 3<sup>rd</sup> Ed., McGraw-Hill, London, p.361, 1977.
15. Whitney, J. M. and Pagano, N. J., "Shear Deformation in Heterogeneous Anisotropic Plates," *Journal of Applied Mechanics*, 1970, pp. 1031-1036.
16. Press, W. H., Teukolsky, S. A., Vetterling, W. T., Flannery, B. P., *Numerical Recipes in FORTRAN. The Art of Scientific Computing*, Cambridge University Press, pp. 1-42, 1992.
17. Akai, T. J., *Applied Numerical Methods for Engineers*, John Wiley & Sons, Inc., New York, pp. 289-313, 1994.
18. Geers, T. L., "Residual Potential and Approximate Methods for Three-Dimensional Fluid-Structure Interaction Problems," *Journal of the Acoustic Society of America*, Vol. 49, 1971, pp. 1505-1510.
19. Huang, H., "Transient Interaction of Plane Waves with a Spherical Elastic Shell," *Journal of the Acoustic Society of America*, Vol. 45, pp. 661-670, 1969.
20. Fox, P. K., (1992) Nonlinear Dynamic Response of Cylindrical Shells Subjected to Underwater Side-On Explosions, Master's Thesis, Naval Postgraduate School, Monterey, California.
21. Rousseau, M. P., (1993) Dynamic Response of a Filament Wound Composite Cylinder Exposed to Underwater Shock, Master's Thesis, Naval Postgraduate School, Monterey, California.
22. Kwon, Y. W., "Thermo-Elastoviscoplastic Finite Element Plate Bending Analysis of Composites," *Engineering Computations*, Vol. 9, pp. 595-607, July 1992.
23. Kwon, Y. W., "Calculation of Effective Moduli of Fibrous Composites with Micromechanical Damage," *Composite Structures*, Vol. 25, pp. 187-192, 1993.
24. Berner, J. M., (1993) Finite Element Analysis of Damage in Fibrous Composites Using a Micromechanical Model, Master's Thesis, Naval Postgraduate School, Monterey, California.

## INITIAL DISTRIBUTION LIST

	No. Copies
1. Defense Technical Information Center Cameron Station Alexandria VA 22304-6145	2
2. Library, Code 052 Naval Postgraduate School Monterey CA 93943-5101	2
3. Professor Young W. Kwon, Code ME/Kw Department of Mechanical Engineering Naval Postgraduate School Monterey CA 93943-5000	2
4. Professor Young S. Shin, Code ME/Sg Department of Mechanical Engineering Naval Postgraduate School Monterey CA 93943-5000	2
5. Department Chairman, Code ME/Kk Department of Mechanical Engineering Naval Postgraduate School Monterey CA 93943-5000	1
6. Naval Engineering Curricular Office, Code 34 Naval Postgraduate School Monterey CA 93943-5000	1
7. Erik A. Rasmussen Code 1720.4 Naval Surface Warfare Center, Carderock Division Bethesda MD 20084-5000	1
8. Lt. Robert Burgio 2913 Ordway Drive Ellicott City MD 21042	2